

# Wrench Control of Dual-Arm Robot on Flexible Base with Supporting Contact Surface

Jeongseob Lee, Doyoon Kong, Hojun Cha, Jeongmin Lee, Dongseok Ryu, Hocheol Shin and Dongjun Lee

**Abstract**—We propose a novel high-force/high-precision interaction control framework of a dual-arm robot system on a flexible base, with one arm holding, or making contact with, a supporting surface, while the other arm can exert any arbitrary wrench in a certain polytope through a desired pose against environments or objects. Our proposed framework can achieve high-force/precision tasks by utilizing the supporting surface just as we humans do while taking into account various important constraints (e.g., system stability, joint angle/torque limits, friction-cone constraint, etc.) and the passive compliance of the flexible base. We first design the control as a combination of: 1) nominal control; 2) active stiffness control; and 3) feedback wrench control. We then sequentially perform optimizations of the nominal configuration (and its related wrenches) and the active stiffness control gain. We also design the PI (proportional-integral) type feedback wrench control to improve the robustness and precision of the control. The key theoretical enabler for our framework is a novel stiffness analysis of the dual-arm system with flexibility, which, when combined with certain constraints, provides some peculiar relations, that can effectively be used to significantly simplify the optimization problem-solving and to facilitate the feedback wrench control design by manifesting the compliance relation at the interaction port. **The efficacy of the theory is then validated and demonstrated through simulations and experiments.**

**Index Terms**—Dual-arm manipulator, flexible base, compliance control, force control, supporting contact, wrench polytope

## NOMENCLATURE

$n$	$\in \mathbb{N}^+$	Dimension of the dual-arm robot on flexible base
$n_a, n_f$	$\in \mathbb{N}^+$	Dimension of actuated joints and the flexible base of the system
$n_e, n_c$	$\in \mathbb{N}^+$	Dimension of the task space and the supporting contact space
$q$	$\in \mathbb{R}^n$	Joint configuration of the dual-arm robot
$q_a, \tau_a$	$\in \mathbb{R}^{n_a}$	Joint configuration and the control actuation of actuated joints of the system
$q_f, \tau_f$	$\in \mathbb{R}^{n_f}$	Joint configuration and the compliance of the flexible base

This research is supported by the Industrial Strategic Technology Development Program (10060070) of the Ministry of Trade, Industry & Energy (MOTIE) of Korea, and the National Research Foundation of Korea (NRF) grant funded by the Korea government (MSIT) (No. NRF2020R1A2C3010039). (*Corresponding author: Dongjun Lee.*)

Jeongseob Lee, Doyoon Kong, Hojun Cha, Jeongmin Lee and Dongjun Lee are with the Department of Mechanical Engineering, IAMD and IOER, Seoul National University, Seoul, Republic of Korea, 08826. {e-mail: overjs94, doyoon99, hjcha23, ljmlgh, djlee}@snu.ac.kr

Dongseok Ryu and Hocheol Shin are with the Korea Atomic Energy Research Institute, Daejeon, Republic of Korea, 34057. {e-mail: sayryu, smarhch}@kaeri.re.kr

$B_f, K_f$	$\in \mathbb{R}^{n_f \times n_f}$	Damping and stiffness matrices of the flexible base
$\xi_e(q), f_e$	$\in \mathbb{R}^{n_e}$	Task pose and respective task wrench
$\xi_c(q), f_c$	$\in \mathbb{R}^{n_c}$	Supporting contact pose and respective contact wrench
$J_e(q)$	$\in \mathbb{R}^{n_e \times n}$	Task space Jacobian matrix
$J_c(q)$	$\in \mathbb{R}^{n_c \times n}$	Contact space Jacobian matrix
$\mathcal{X}_c$		Supporting environment
$\mathcal{W}_e^d$		Task wrench polytope
$f_e^*$	$\in \mathbb{R}^{n_e}$	Nominal task wrench
$q^*$	$\in \mathbb{R}^n$	Nominal joint configuration
$f_c^*$	$\in \mathbb{R}^{n_c}$	Nominal contact wrench
$\tau_a^*$	$\in \mathbb{R}^{n_a}$	Nominal control actuation
$\tau_a^k$	$\in \mathbb{R}^{n_a}$	Active compliance control actuation
$B_a, K_a$	$\in \mathbb{R}^{n_a \times n_a}$	Damping and stiffness active control gain
$\tau_a'$	$\in \mathbb{R}^{n_a}$	Feedback wrench control actuation
$\bar{K}, \bar{K}_{geo}$	$\in \mathbb{R}^{n \times n}$	Effective stiffness and geometric stiffness

## I. INTRODUCTION

INDUSTRIAL facilities often require regular inspection and emergency maintenance to ensure effective performance and safety. These maintenance tasks involve operations in the height environment, such as nuclear fuel magazine replacement, live-wire powerline maintenance, and other infrastructure maintenance tasks in various industrial fields. Despite the availability of skilled workers, these tasks are inherently dangerous, often resulting in fatalities and injuries. Thus, robotization has become increasingly desirable and has been actively sought by many companies and research groups [1]–[5] (see Fig. 1).

However, robotizing such tasks presents significant challenges, as extending platforms to reach high altitudes often results in substantial flexibility. This flexibility arises from the compliance of the components (e.g., the flexibility of each link of the telescoping platform) as well as the assembly tolerances between the components (e.g., gaps at the joints of the telescoping platform). These factors accumulate along the length of the extending platform, leading to considerable deformation and oscillation at the end of the platform. Since the target maintenance task requires high-force and high-precision operations (e.g., releasing the magazine, precision cutting and pushing-insertion of wire into connectors, pushing or pulling of infrastructure equipment, and industrial tool manipulation such as drilling and hammering), managing the flexibility-induced deformation and oscillation becomes an even more critical concern.

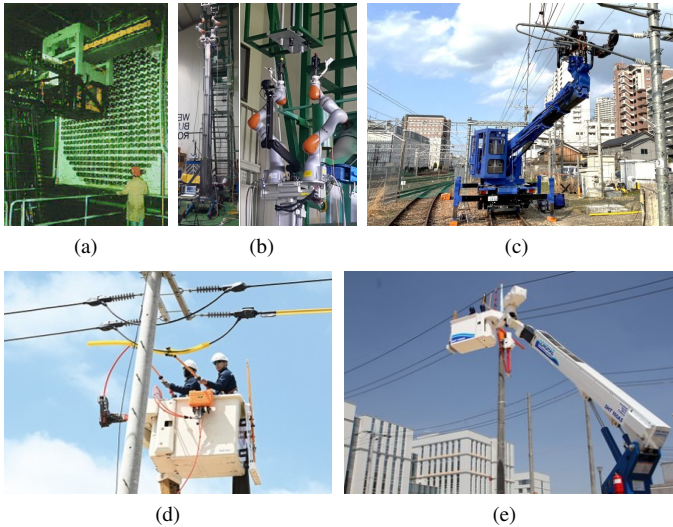


Fig. 1: Examples of industrial operation and robotization for height environment operation. (a) Fuel replacement in nuclear power plants. (b) Dual-arm telerobotic system for fuel replacement in nuclear power plant [1]–[3]. (c) JR-West humanoid robot for railway infrastructure maintenance [4]. (d) Live-wire powerline maintenance. (e) Dual-arm robot system for live-wire powerline maintenance [5].

In this paper, we consider the problem of how to achieve high-force/high-precision in-height robot operation on an extending platform with substantial end-flexibility. For this, we specifically consider the set-up of a dual-arm robot system on the flexible base as described in Fig. 2 with a **support-providing surface**. Inspired by the exploitation of supporting contact/surface by humans in daily life, we aim to attain high-force/high-precision operation by one (right/working/interaction) arm while holding, or pushing on, the surface by the other (left/supporting/contact) arm. We also specify the target task as to generate any wrench in a desired task wrench set at the right arm against the task environment, while holding the surface or maintaining the bilateral/holding or unilateral/frictional contact on the supporting surface by the left arm. The desired task wrench set is defined by the form of wrench polytope denoted by  $\mathcal{W}_e^d$ . Recruiting the left arm to utilize the supporting contact is crucial, since, without that, it would be difficult to precisely regulate the high-interaction wrench by the right arm, as the (often lightly-damped) flexible base may produce oscillation or even its deformation may be too large to hold against the high-interaction wrench at the right arm. Here, note that the system we consider is under-actuated: only the two robot arms are fully-actuated, while the flexible base lacks any control actuation.

To solve this problem, we design our control to be composed of the nominal control  $\tau_a^*$  (to produce centroid of  $\mathcal{W}_e^d$ ), the active stiffness control  $\tau_a^k$  with the stiffness gain  $K_a$ , and the real-time feedback wrench control  $\tau_a'$  to improve precision and robustness of the interaction wrench control at the right hand. More precisely, we first optimize the normal configuration  $q^*$  of the total system (i.e., two robot arms and the flexible base), the nominal control actuation  $\tau_a^*$  of the two arms and the nominal supporting contact wrench  $f_c^*$  at the left arm to

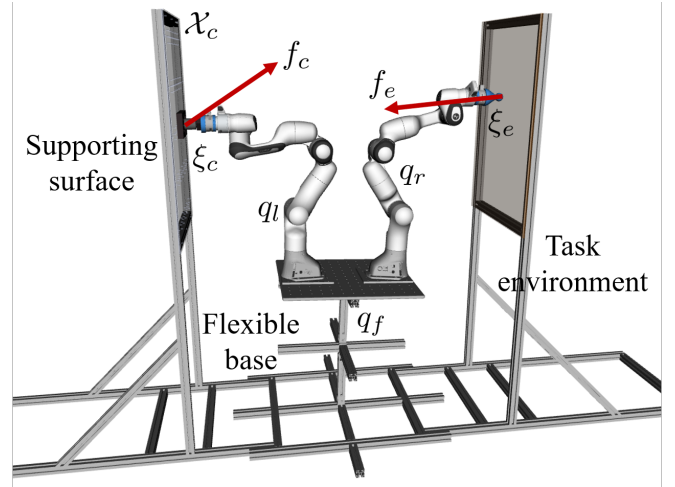


Fig. 2: The interaction task of the dual-arm robotic system on the flexible base utilizing supporting contact. The system performs interaction tasks with one arm while maintaining supporting contact with the other arm.

produce the representative/nominal task wrench  $f_e^*$  (i.e., the centroid of  $\mathcal{W}_e^d$ ) at the right arm, while minimizing the nominal control  $\tau_a^*$  and also ensuring the stability of the interaction operation by alleviating the possibly-destabilizing effect of geometric stiffness [6], [7], all under the supporting surface holding/frictional-contact constraints and the limits of the joint angles and control actuation constraints. This optimization is then followed by the second optimization to choose the active stiffness gain  $K_a$  for  $\tau_a^k$ , under the constraints that the overall stiffness of the system (i.e., combination of flexible base stiffness  $K_f$ , active stiffness gain  $K_a$ , and geometric stiffness  $\bar{K}_{geo}$ ) to be positive-definite (for system stability) and the desired wrench polytope  $\mathcal{W}_e^d$  to be compatible with the constraints of the joint torque limits and the supporting contact maintenance (e.g., friction-cone constraint). Finally, the feedback wrench control  $\tau_a'$  is designed based on the stiffness relation at the right arm end-effector with the effect of  $\tau_a'$  fully analyzed. **The robustness and the stability of the proposed control framework are also formally analyzed and established in the presence of uncertainties. See Fig. 3 for the overall architecture of the proposed control framework.**

The key theoretical result to allow us to attain these is the novel stiffness analysis of the dual-arm robot on the flexible base. More precisely, through some variational analysis under the supporting contact maintenance constraint<sup>1</sup>, we could extract a peculiar stiffness relation linear among  $\delta f_c, \delta f_e, \delta \tau_a$  (i.e., deviations of  $f_c, f_e, \tau_a$  around the nominal configuration and wrenches  $q^*, f_e^*, f_c^*, \tau_a^*$ ). This relation is particularly crucial for our second optimization process, as it allows us to explicitly compute the effect of the supporting-contact wrench constraints (i.e.,  $\mathcal{W}_e^c$ ) and the control actuation limits (i.e.,  $\mathcal{W}_e^l$ ) at the right arm wrench space so that we can efficiently check if the desired wrench polytope  $\mathcal{W}_e^d$  at the right arm is feasible with those constraints/limits. Using this linear

<sup>1</sup>This holding/contact-maintenance constraint is ensured by explicitly incorporating its relevant constraints into our optimization formulation with some safety-margin at the supporting-contact polytopes to address the effect of  $\tau_a'$

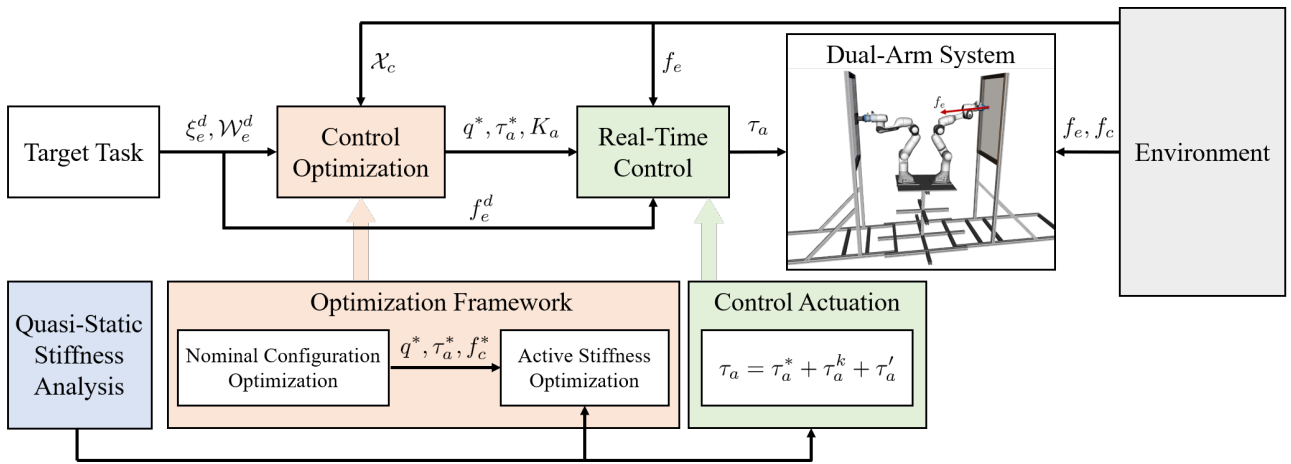


Fig. 3: The schematic diagram of the proposed control framework.

relation, we can also eliminate a substantive number of search variables, thereby, significantly improving the computational efficiency and convergence of the optimization solving. This relation also enables us to extract the stiffness equation at the right arm wrench space, thereby, greatly facilitating our design of the feedback wrench control  $\tau_a'$ .

Arising from the aforementioned challenges and the proposed methodologies, the contributions of this paper can be articulated as follows:

- 1) We propose a novel control framework utilizing a supporting surface, which integrates nominal control, active stiffness control, and real-time feedback wrench control. These control actuations are calculated through the two-stage sequential optimization together with its related wrenches. We also provide the formal robustness and stability proof of the proposed control framework in the presence of uncertainties.
- 2) A novel stiffness analysis to extract linear relation among deviations of control actuation and related wrenches. This relation, which is derived under the contact constraint, enables us to improve the computing efficiency of the optimization and the design of the feedback wrench control.
- 3) The efficacy of the proposed control framework is validated through extensive evaluation including simulation and experiment for the dual-arm telerobotic system for nuclear power plant [1]–[3] (Fig. 1b) and the dual-arm system setup on the flexible base (Fig. 2).

There has been a long history of research into the control problem of single or dual robot manipulators on a flexible base. These studies cover various types of manipulator systems on a flexible base, for instance, flexible-macro/rigid-micro manipulator systems [8]–[12], single manipulator systems mounted on a flexible fixed base [13]–[19], manipulator systems on a flexible wheeled mobile robot [20], [21], manipulator systems on a flexible beam with additional actuation [2], [3], and dual-arm humanoid systems on flexible mobile base [22]. However, all of these results [2], [3], [8]–[22] focus on the problem of vibration suppression for the pure precise motion control without any environmental interaction. While there has been

some progress in force control for single manipulator systems on flexible fixed bases [23], [24] and in flexible-macro/rigid-micro manipulator systems [25], these studies are generally limited to a single manipulator system on a linearized flexible base with only one or two degrees of freedom (DOFs).

The problem of high-force interaction control has been actively explored for the manipulator system on the rigid base including contact-rich manipulation planning [26], hybrid motion-force control [27], and nonprehensile manipulation [28], [29]. However, these results mainly focus on end-effector task space dynamics without considering base dynamics modeling. In the field of legged robot systems, the problem of high-force interaction has been explored across various platforms, including quadruped systems [30]–[37] and humanoid systems [38]–[46]. These studies cover various types of high-force interaction including heavy-object pushing [30]–[33], [37], [39]–[42], object transportation [34]–[36], wall pushing [33], [38], soil digging [43]–[45] and valve turning [46]. However, these approaches primarily execute interaction forces in a feedforward manner, which does not fully account for uncertainties and disturbances during environmental interactions. Furthermore, most of these results mainly rely on the reduced dynamics (e.g., centroidal dynamics [47], [48]), which is typically adopted for the control of humanoid robots due to their high-DOFs, yet, fundamentally inapplicable for analyzing the effect of the flexibility. In contrast, our framework proposed in this paper is based on the full dynamics analysis of the system to manifest the complete effect of flexibility on the system behavior. As far as we know, our result in this paper is the very first result for the high-force/high-precision interaction task control of the dual-arm system on the flexible base.

The rest of the paper is organized as follows: Sec. II shows problem formulation for our control framework. Quasi-static stiffness analysis and a linear relation among  $(\delta f_c, \delta f_e, \delta \tau_a)$  are described in Sec. III. Based on this linear relation, Sec. IV provides stiffness analysis at the interaction task space and the feedback wrench control. Sec. V provides details of a nominal configuration and active stiffness optimization. Formal robustness analysis and stability proof in the presence of uncertainties is given in Sec. VI. Sec. VII presents evaluation

results demonstrating the efficacy of our control framework through simulations and experiments on two different dual-arm systems on flexible bases. Discussions on the limitations of the current framework and future work directions are provided in Sec. VIII. Finally, Sec. IX concludes the paper.

## II. PROBLEM FORMULATION

### A. System Modeling

Consider the dual-arm manipulator system on the flexible base as shown in Fig. 2, whose dynamics can be expressed by

$$\begin{aligned} M(q)\ddot{q} + C(q, \dot{q})\dot{q} + G(q) + \mathcal{S}_f \tau_f \\ = \mathcal{S}_a \tau_a - J_c^T(q) f_c + J_e^T(q) f_e \end{aligned} \quad (1)$$

where  $q = [q_f; q_a] \in \mathbb{R}^n$  is the system configuration with  $q_f \in \mathbb{R}^{n_f}$  and  $q_a = [q_i; q_r] \in \mathbb{R}^{n_a}$  respectively being the configurations of the flexible base and that of the actuated joints of the dual-arm manipulator;  $M(q)$ ,  $C(q, \dot{q}) \in \mathbb{R}^{n \times n}$ , and  $G(q) \in \mathbb{R}^n$  are the inertia, Coriolis, and gravity matrices of the system;  $\tau_f$  is the compliance of the (un-actuated) flexible base as given by

$$\tau_f = B_f(q_f)\dot{q}_f + K_f(q_f)[q_f - q_f^0] \quad (2)$$

where  $B_f(q_f) \in \mathbb{R}^{n_f \times n_f}$  and  $K_f(q_f) \in \mathbb{R}^{n_f \times n_f}$  are the damping and stiffness matrices with  $q_f^0 \in \mathbb{R}^{n_f}$  being an equilibrium configuration; and  $\tau_a \in \mathbb{R}^{n_a}$  is the control actuation for the (fully-actuated) dual-arm robots, which is to be designed below.

**Assumption 1.** *As shown in Fig. 2, the right arm is performing the high-force/precision interaction tasks against an environment (or object), while the left arm is holding, or maintaining the contact on, the supporting surface  $\mathcal{X}_c$ .*

Their respective poses and task/contact wrenches are then given by  $\xi_e(q) \in \mathbb{R}^{n_e}$ ,  $\xi_c(q) \in \mathbb{R}^{n_c}$  and  $f_e \in \mathbb{R}^{n_e}$  and  $f_c \in \mathbb{R}^{n_c}$ , with  $\dot{\xi}_e(q) = J_e(q)\dot{q}$  and  $\dot{\xi}_c(q) = J_c(q)\dot{q}$ , where  $J_e(q) \in \mathbb{R}^{n_e \times n}$  and  $J_c(q) \in \mathbb{R}^{n_c \times n}$  are the end-effector and supporting-contact Jacobian matrices of the right and left arms. The matrices  $\mathcal{S}_f \in \mathbb{R}^{n \times n_f}$  and  $\mathcal{S}_a \in \mathbb{R}^{n \times n_a}$  are the selection matrices as defined by

$$\mathcal{S}_f = \begin{bmatrix} I_{n_f} \\ 0_{n_a \times n_f} \end{bmatrix} \in \mathbb{R}^{n \times n_f}, \quad \mathcal{S}_a = \begin{bmatrix} 0_{n_f \times n_a} \\ I_{n_a} \end{bmatrix} \in \mathbb{R}^{n \times n_a} \quad (3)$$

**Assumption 2.** *In this paper, for simplicity, we assume constant compliance parameters  $B_f$  and  $K_f$  with the zero equilibrium configuration  $q_f^0 = 0$ . The obtained results however can be easily extended for variable compliance and non-zero equilibrium of the flexible base.*

**Assumption 3.** *As typically true for high-force/high-precision tasks, we assume that the system motion is slow enough so that the system dynamics (1) can be suitably captured by the following quasi-static equation:*

$$G(q) + \mathcal{S}_f K_f q_f = \mathcal{S}_a \tau_a - J_c^T(q) f_c + J_e^T(q) f_e \quad (4)$$

Here, note that this equation (4) is under-actuated (i.e., fully-actuated dual-arm with un-actuated flexible base with  $n = n_a + n_f$ ). Further, the actuation  $\tau_a \in \mathbb{R}^{n_a}$  is not in the same

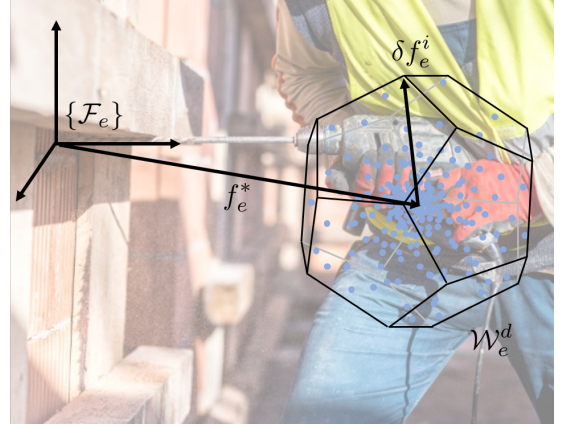


Fig. 4: The set of target task wrench data can be reformulated to the form of a desired wrench polytope  $\mathcal{W}_e^d$  with its center  $f_e^*$  and  $n_p$  apex wrench vectors  $\delta f_e^i$ .

space with the interaction force  $f_e \in \mathbb{R}^{n_e}$  or the contact force  $f_c$ , thus, how to affect the interaction and contact forces via the control  $\tau_a$  is not straightforward.

### B. Control Objectives

In this paper, we aim to achieve the following control objectives at the same time:

- The right arm end-effector should be capable of exerting any desired wrench against the environment within the task wrench polytope as defined by

$$\mathcal{W}_e^d = \{f_e \in \mathbb{R}^{n_e} | f_e = f_e^* + \sum_{i=1}^{n_p} \alpha_i \delta f_e^i, \alpha_i \geq 0, \sum_{i=1}^{n_p} \alpha_i \leq 1\} \quad (5)$$

while maintaining the desired pose  $\xi_e(q) = \xi_e^d$ , where  $f_e^*$  is the nominal task wrench around the nominal configuration  $q^* \in \mathbb{R}^n$  (to be defined below), which is also the centroid of  $\mathcal{W}_e^d$  with  $n_p$  apex wrench vectors  $\delta f_e^i$  and weight factor  $\alpha_i$  satisfying  $\alpha_i \geq 0$  and  $\sum_{i=1}^{n_p} \alpha_i \leq 1$ . This polytope is formulated based on the set of task wrench data (see Fig. 4).

- During this operation, the left arm end-effector should hold, or maintain the contact with, the supporting surface  $\mathcal{X}_c$  with  $\xi_c(q) \in \mathcal{X}_c \forall t \geq 0$ , while contact wrench  $f_c$  constrained to be in the set of

$$\mathcal{W}_c := \{f_c \in \mathbb{R}^{n_c} | \|f_c\|_\infty \leq \alpha\} \quad (6)$$

for the case of bilateral holding (e.g., rigidly grip a bar, fixed to the surface via bolting) with bounded contact force; or in the set of

$$\mathcal{W}_c := \{f_c \in \mathbb{R}^{n_c} | f_c^t \leq \mu f_c^n, f_c^n \geq 0\} \quad (7)$$

for the case of unilateral/friction-cone contact, where  $f_c^n = (f_c \cdot n_c)n_c$  and  $f_c^t = f_c - f_c^n$  are normal and tangential contact forces for the contact surface normal  $n_c$ , and  $\mu$  is the friction coefficient.

- We aim to achieve the objectives above, while also ensuring the stability of (4) against perturbation around the

normal configuration  $q^*$  (to be defined below), respecting the joint angle and torque limits s.t.,

$$\underline{q} < q^* < \bar{q} \quad (8)$$

$$\underline{\tau}_a \leq \tau_a^* \leq \bar{\tau}_a \quad (9)$$

and utilizing the passive stiffness  $K_f$  of the flexible base as much as possible.

To achieve these control objectives, we design the control actuation  $\tau_a$  s.t.,

$$\tau_a = \tau_a^* + \tau_a^k + \tau_a' \quad (10)$$

with each term explained as follows:

- The first term  $\tau_a^*$  is the nominal control to generate the nominal task wrench  $f_e^* \in \mathcal{W}_e^d$  and the nominal contact wrench  $f_c^* \in \mathcal{W}_c$  at the nominal equilibrium configuration  $q^*$  with

$$G(q^*) + \mathcal{S}_f K_f q_f^* = \mathcal{S}_a \tau_a^* - J_c^T(q^*) f_c^* + J_e^T(q^*) f_e^* \quad (11)$$

where  $q^* = [q_f^*; q_a^*] \in \mathbb{R}^n$  will be computed via the optimization process in Sec. V-A to satisfy the control objectives as stated above;

- The second term is given by

$$\tau_a^k := -B_a \dot{q}_a - K_a [q_a - q_a^*] \quad (12)$$

which is the active compliance control to stabilize the system (4) and enhance the robustness around the equilibrium  $q^*$ , where  $B_a, K_a \in \mathbb{R}^{n_a \times n_a}$  are the damping and stiffness gains. Only the stiffness gain  $K_a$  we will consider here, and will be chosen via the optimization procedure in Sec. V-B while ensuring the system stability and the task and supporting-contact wrench requirements (i.e.,  $f_e \in \mathcal{W}_e^d$  and  $f_c \in \mathcal{W}_c$ ), for which the peculiar linear relation among  $\delta f_c, \delta f_e, \delta \tau_a$  (i.e., deviations of  $f_c, f_e, \tau_a$  around  $q^*, f_c^*, f_e^*, \tau_a^*$ ) to be obtained in Sec. III-B turns out to greatly facilitate the optimization formulation and solving of Sec. V-B; and

- The last term  $\tau_a'$  is to contain the PI (proportional-integral) type control with the feedback of the task wrench  $f_e$  to precisely track the desired wrench  $f_e^d \in \mathcal{W}_e^d$  while enhancing the control robustness in general via the feedback action. **Thanks to the aforementioned linear relation among  $\delta f_c, \delta f_e, \delta \tau_a$ , we can facilitate the design of  $\tau_a'$  as described in Sec. IV.**

### III. STIFFNESS ANALYSIS AND POLYTOPE MAPPINGS

In this section, by perturbing (4), we analyze the stiffness of the system (4) around the nominal equilibrium  $(q^*, f_e^*, f_c^*)$  of (11). The perturbation analysis provides a linear relation among the deviations  $\delta q, \delta f_e, \delta f_c$  and  $\delta \tau_a := \tau_a^k + \tau_a'$ , respectively from  $q^*, f_e^*, f_c^*$  and  $\tau_a^*$ . This linear relation, combined with the contact-maintaining/surface-holding constraint  $\xi_c(q) \in \mathcal{X}_c$ , then allows us to map the contact wrench polytope  $\mathcal{W}_c$  in (6)-(7) and the torque limit polytope (9) into the space of the interaction wrench  $f_e$ , thereby, allowing us to check their effects on the attainment of exerting the desired wrench by the right-arm (i.e.,  $f_e^d \in \mathcal{W}_e^d$ ) in a straightforward manner (see the optimization of  $K_a$  in Sec. V-B). This relation further

reveals the stiffness relation at the right-arm end-effector (i.e., between  $\delta \xi_e$  and  $\delta f_e$ ), which turns out to be instrumental for our design of the feedback control  $\tau_a'$  (see Sec. IV).

#### A. Perturbation Analysis and Stiffness Matrices

By perturbing (11) around the nominal equilibrium  $(q^*, f_e^*, f_c^*)$  with the control equation (10) and (12), we have

$$\begin{aligned} G(q^* + \delta q) + \mathcal{S}_f K_f [q_f^* + \delta q_f] + J_c(q^* + \delta q)^T [f_c^* + \delta f_c] \\ = \mathcal{S}_a [\tau_a^* - K_a \delta q_a + \tau_a'] + J_e(q^* + \delta q)^T [f_e^* + \delta f_e] \end{aligned} \quad (13)$$

where  $\delta q, \delta f_e, \delta f_c$  are the deviations around the nominal state. Taking the first-order Taylor expansion, we can get

$$\begin{aligned} G(q^*) + \frac{\partial G(q)}{\partial q} \Big|_{q^*} \delta q + \mathcal{S}_f K_f [q_f^* + \delta q_f] \\ + J_c^T(q^*) [f_c^* + \delta f_c] + \frac{\partial J_c^T(q) f_c^*}{\partial q} \Big|_{q^*} \delta q \\ = \mathcal{S}_a [\tau_a^* - K_a \delta q_a + \tau_a'] \\ + J_e^T(q^*) [f_e^* + \delta f_e] + \frac{\partial J_e^T(q) f_e^*}{\partial q} \Big|_{q^*} \delta q \end{aligned} \quad (14)$$

From this, we can obtain a linear stiffness equation of the system around the equilibrium (11) s.t.,

$$\bar{K} \delta q + J_c^T(q^*) \delta f_c = J_e^T(q^*) \delta f_e + \mathcal{S}_a \tau_a' \quad (15)$$

with  $\bar{K} \in \mathbb{R}^{n \times n}$  being the effective stiffness of the system (4) as given by

$$\bar{K} := \bar{K}_f + \bar{K}_a + \bar{K}_{geo} \quad (16)$$

where  $\bar{K}_f = \mathcal{S}_f K_f \mathcal{S}_f^T$  is the passive stiffness (from the flexible base),  $\bar{K}_a = \mathcal{S}_a K_a \mathcal{S}_a^T$  is the active stiffness (from  $K_a$  of (12)), and

$$\bar{K}_{geo} := \left[ \frac{\partial G(q)}{\partial q} \Big|_{q^*} + \frac{\partial J_c^T(q) f_c^*}{\partial q} \Big|_{q^*} - \frac{\partial J_e^T(q) f_e^*}{\partial q} \Big|_{q^*} \right] \quad (17)$$

is the geometric stiffness [6], [7]. The geometric stiffness  $\bar{K}_{geo}$  is not necessarily positive-definite, thus, can induce system instability. On the other hand, this  $\bar{K}_{geo}$  not only depends on  $q^*$ , but also  $f_c^*$  and  $f_e^*$ . For this, in the optimization process of Sec. V-A, we aim to minimize the effect of this possibly-destabilizing  $\bar{K}_{geo}$  by optimizing  $q^*$  and  $f_c^*$ , so that it can be dominated by the positive-definite (i.e., always stabilizing)  $\bar{K}_f$  and  $\bar{K}_a$ , which would be granted in practice with a reasonably-designed flexible base (i.e., not so soft with large enough  $K_f$ ) and a reasonably-strong dual robotic arms (i.e., large enough  $K_a$  possible for (12)), as also evidenced in Sec. VII-B. Note also that, although not included in the analysis here, the damping gain  $B_a$  of (12) always helps the system stability.

#### B. Polytope Mappings under $\xi_c(q) \in \mathcal{X}_c$

Now, given  $(f_e^*, f_c^*, \tau_a^*)$  from (11), if we can analyze the behavior of the deviations  $(\delta f_e, \delta f_c, \delta \tau_a)$ , we would be able to see if the interaction task is attained (i.e.,  $f_e^d = f_e^* + \delta f_e$ ) and the supporting-contact constraint (i.e.,  $f_c = f_c^* + \delta f_c \in \mathcal{W}_c$

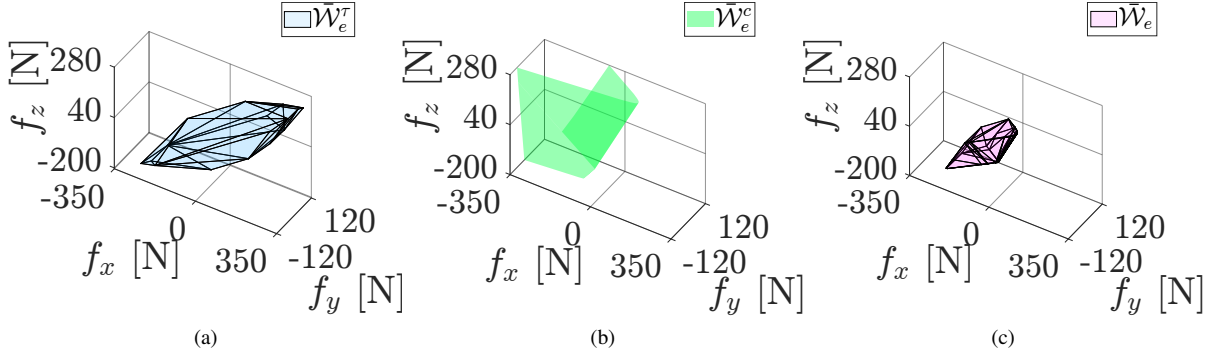


Fig. 5: Example of the polytope mappings under the supporting contact constraint: (a) Formulation of  $\bar{\mathcal{W}}_e^\tau$ . (b) Formulation of  $\bar{\mathcal{W}}_e^c$  for unilateral/friction-cone contact. (c) Formulation of  $\bar{\mathcal{W}}_e := \bar{\mathcal{W}}_e^\tau \cap \bar{\mathcal{W}}_e^c$ .

with (6)-(7)) or the joint torque limit constraint (i.e.,  $\tau_a = \tau_a^* + \delta\tau_a = \tau_a^* + \tau_a^k + \tau_a^l$  with (9)) is violated. Also, since what we ultimately want is to achieve the interaction task at the right arm, it would be useful and convenient to map the supporting-contact constraint  $\mathcal{W}_c$  and the joint torque limit constraint (9) into the task wrench space of  $f_e$ , and see how those constraints will curb the possible wrench-generation polytope at the right arm.

For this, here, we utilize the constraint that  $\xi_c(q) = \mathcal{X}_c$ , which is granted *at default* if the left arm is rigidly holding the supporting surface with (6) or will (and needs to) be enforced by the optimization processes in Sec. V if the left-arm is to maintain the frictional contact on the surface with (7). Then, the penetration into the supporting-surface  $\mathcal{X}_c$  should be zero, or we should have:

$$\begin{aligned} \delta\xi_c &= J_c(q^*)\delta q \\ &= J_c(q^*)\bar{K}^{-1}[-J_c^T(q^*)\delta f_c + J_e^T(q^*)\delta f_e + \mathcal{S}_a\tau_a'] \equiv 0 \end{aligned} \quad (18)$$

where we use (15). From this, we can obtain

$$\delta f_c = J_c^{\bar{K}+T}(q^*)[J_e^T(q^*)\delta f_e + \mathcal{S}_a\tau_a'] \quad (19)$$

where  $J_c^{\bar{K}+T}(q^*) = \bar{K}^{-1}J_c^T(q^*)[J_c(q^*)\bar{K}^{-1}J_c^T(q^*)]^{-1} \in \mathbb{R}^{n \times n_c}$  is the weighted pseudo inverse of  $J_c(q^*)$  w.r.t. the effective stiffness  $\bar{K}$ . Injecting (19) into (15), we then have

$$\bar{K}\delta q = N_c(q^*)[J_e^T(q^*)\delta f_e + \mathcal{S}_a\tau_a'] \quad (20)$$

where the term  $J_e^T(q^*)\delta f_e$  is projected to the space, which cannot be supported by  $J_c^T(q^*)$  with the associated null-space operator  $N_c(q^*) \in \mathbb{R}^{n \times n}$  w.r.t. the effective stiffness  $\bar{K}$  given by

$$N_c(q^*) = I - J_c^T(q^*)J_c^{\bar{K}+T}(q^*)$$

Using (20) in (10), we can express the control (10) as a function of  $\delta f_e$  s.t.,

$$\begin{aligned} \tau_a &= \tau_a^* - K_a\delta q_a + \tau_a^l = \tau_a^* - K_a\mathcal{S}_a^T\delta q + \tau_a^l \\ &= \tau_a^* - K_a\mathcal{S}_a^T\bar{K}^{-1}N_c(q^*)[J_e^T(q^*)\delta f_e + \mathcal{S}_a\tau_a'] + \tau_a^l \end{aligned} \quad (21)$$

This relation (21) then allows us to map the joint torque limit constraint (9) into the following  $\tau$ -polytope in the task wrench space of the right arm:

$$\mathcal{W}_e^\tau := \{f_e \in \mathbb{R}^{n_e} \mid \tau_a \leq A_\tau + B_\tau\delta f_e + C_\tau\tau_a^l \leq \bar{\tau}_a\} \quad (22)$$

where  $f_e = f_e^* + \delta f_e$  with  $f_e^*$  given, and  $(A_\tau, B_\tau, C_\tau)$  are suitably defined from (21). This mapping from (9) to the polytope  $\mathcal{W}_e^\tau$  is possible due to the linear relation between  $\tau_a$  and  $\delta f_e$  in (21). Note also the presence of  $\tau_a^l$ , which is a feedback control, thus, cannot be known *a priori*. This term  $\tau_a^l$ , yet, is typically boundedness in practice. Let us denote its bound through the operator  $C_\tau$  by  $\mathcal{B}_{\epsilon_1}$ . We choose this  $\mathcal{B}_{\epsilon_1}$  to be constant (e.g., independent from  $K_a$ ). This can be possible if we compute its conservative estimate with the various bounds taken into account. A necessary condition for the control objective of exerting any  $f_e \in \mathcal{W}_e^d$  by the right arm is then given by

$$\mathcal{W}_e^d \oplus \mathcal{B}_{\epsilon_1} \subset \bar{\mathcal{W}}_e^\tau \quad (23)$$

where  $\oplus$  is the Minkowski sum operator and  $\bar{\mathcal{W}}_e^\tau := \{f_e \in \mathbb{R}^{n_e} \mid \tau_a \leq A_\tau + B_\tau\delta f_e \leq \bar{\tau}_a\}$  (i.e., nominal  $\tau$ -polytope with  $\tau_a^l \equiv 0$  in (22)). See Sec. IV for more details on the boundedness of  $\tau_a^l$ .

On the other hand, similarly to (22), using (19), we can express the supporting-contact wrench in the task wrench space of the right arm s.t.,

$$f_c = f_c^* + J_c^{\bar{K}+T}[J_e^T(q^*)\delta f_e + \mathcal{S}_a\tau_a'] \quad (24)$$

where the contact wrench  $f_c$  should be in the set of  $\mathcal{W}_c$  as given in (6) or (7). This condition can be expressed by

$$\mathcal{W}_e^c := \{f_e \in \mathbb{R}^{n_e} \mid A_c + B_c\delta f_e + C_c\tau_a^l \in \mathcal{W}_c\} \quad (25)$$

where  $f_e = f_e^* + \delta f_e$  and  $(A_c, B_c, C_c)$  are suitably defined from (24). This then leads into a polytope in the task wrench space of  $f_e$  for the case of (6) or a cone for the case of (7). A necessary condition for the right arm to exert any wrench  $f_e$  in the set of  $\mathcal{W}_e^d$  can then be written by

$$\mathcal{W}_e^d \oplus \mathcal{B}_{\epsilon_2} \subset \bar{\mathcal{W}}_e^c \quad (26)$$

where  $\epsilon_2$  denotes a bound of  $\tau_a^l$  through  $C_c$  and  $\bar{\mathcal{W}}_e^c$  is the nominal contact wrench polytope with  $\bar{\mathcal{W}}_e^c := \{f_e \in \mathbb{R}^{n_e} \mid A_c + B_c\delta f_e \in \mathcal{W}_c\}$ . Similarly for (23) above, here, we also assume this ball  $\mathcal{B}_{\epsilon_2}$  to be of a (conservatively-computed) constant radius. See also Sec. IV for more details on the bounds of  $\tau_a^l$ .

These two inclusion conditions in (23) and (26) should both be satisfied for the task feasibility, and we can define resultant wrench set  $\bar{\mathcal{W}}_e$  by

$$\bar{\mathcal{W}}_e = \bar{\mathcal{W}}_e^r \cap \bar{\mathcal{W}}_e^c \quad (27)$$

An example of  $\bar{\mathcal{W}}_e^r$ ,  $\bar{\mathcal{W}}_e^c$  and  $\bar{\mathcal{W}}_e$  formulation is illustrated in Fig. 5.

Here, note that the two inclusion conditions, (23) and (26), can be checked simply by inserting each  $\delta f_e^i$  of (5) into (23) or (26) to see if any of them violates the condition of (23) or (26). This straightforward checking of the two conditions (23) and (26) is possible thanks to the stiffness analysis presented in this Sec. III and substantially facilitates the optimization solving to find  $K_a$  under these two inclusion conditions in Sec. V-B. Our stiffness analysis presented here also allows us to obtain the stiffness behavior at the right arm end-effector and to design the real-time control  $\tau'_a$  in (10) based on that. This is explained in the following Sec. IV.

#### IV. DESIGN OF FEEDBACK WRENCH CONTROL

Using (20), we can derive the stiffness relation at the right-arm end-effector as follows:

$$\begin{aligned} \delta \xi_e &= J_e(q^*) \delta q \\ &= K_e^{-1} [\delta f_e + K_e(q^*) J_e(q^*) \bar{K}^{-1} N_c(q^*) \mathcal{S}_a \tau'_a] \end{aligned} \quad (28)$$

where

$$K_e(q^*) := [J_e(q^*) \bar{K}^{-1} N_c(q^*) J_e^T(q^*)]^{-1} \in \mathbb{R}^{n_e \times n_e} \quad (29)$$

is the interaction task space stiffness matrix at the right arm. This stiffness matrix  $K_e(q^*)$  is not necessarily symmetric and positive-definite from that  $\bar{K}(q^*)$  in (16) is in general neither due to the presence of  $\bar{K}_{geo}(q^*)$ . It is not so problematic even if  $\bar{K}_e$  is not symmetric, yet, it is definitely so if  $\bar{K}_e$  is not positive-definite, as the system can then exhibit instability. This issue is resolved in the optimization process in Sec. V-B, where we explicitly enforce the positive-definite constraint for  $\bar{K}_e$ .

For the stiffness relation (28), we can design the PI (proportional-derivative) type control  $\tau'_a$  with  $\delta f_e$ -feedback as follows. Let us first rewrite (28) by

$$K_e \delta \xi_e = \delta f_e + \mathcal{S}_e \tau'_a \quad (30)$$

where  $\mathcal{S}_e(q^*) := K_e(q^*) J_e(q^*) \bar{K}^{-1} N_c(q^*) \mathcal{S}_a \in \mathbb{R}^{n_e \times n_a}$ . The wrench control objective is given by

$$f_e = f_e^* + \delta f_e \rightarrow f_e^d = f_e^* + \delta f_e^d \in \mathcal{W}_e^d$$

that is, what we need to attain can be written as  $\delta f_e \rightarrow \delta f_e^d$ . To attain this, we design  $\tau'_a$  s.t.,

$$\tau'_a = \mathcal{S}_e^\dagger [K_e \delta \xi_e - \delta f_e^d + K_I \int_0^t (\delta f_e - \delta f_e^d) ds] \quad (31)$$

where  $K_I \in \mathbb{R}^{n_e \times n_e}$  is the integral control gain and  $\mathcal{S}_e^\dagger = D_\tau \mathcal{S}_e^T (\mathcal{S}_e D_\tau \mathcal{S}_e^T)^{-1} \in \mathbb{R}^{n_a \times n_e}$  is the weighted pseudo inverse of  $\mathcal{S}_e$  with the weight matrix  $D_\tau = \text{diag}[\tau_1^{lim}, \tau_2^{lim}, \dots, \tau_{n_a}^{lim}] \in \mathbb{R}^{n_a \times n_a}$  based on the joint torque limit  $\tau_i^{lim} := \frac{\tau_i - \bar{\tau}_i}{2}$ .

The closed-loop dynamics of (30) under (31) is then given by

$$\delta f_e - \delta f_e^d + K_I \int_0^t (\delta f_e - \delta f_e^d) ds = 0 \quad (32)$$

implying that  $f_e = f_e^d \in \mathcal{W}_e^d$ . This linear exponentially-stable dynamics (32) also implies that  $\tau'_a$  is bounded, even in the presence of uncertainty, unmodeled disturbance, etc. This bound of  $\tau'_a$  is (conservatively) estimated and used to compute  $\epsilon_1, \epsilon_2$  in the inclusion constraints (23) and (26) to ensure their satisfaction even in the presence of  $\tau'_a$  therein.

#### V. NOMINAL CONFIGURATION AND ACTIVE STIFFNESS OPTIMIZATION

In this Sec. V, we present optimization processes to decide the nominal configuration  $q^*$  and the active stiffness gain  $K_a$  of (12) under all the constraints as stated in Sec. II-B while utilizing the passive stiffness  $K_f$  of the flexible base as much as we can. For this, we assume that the nominal right arm pose  $\xi_e$ , the supporting contact surface  $\mathcal{X}_c$ , and the desired wrench polytope  $\mathcal{W}_e^d$  (i.e.,  $f_e^*$  and  $\delta f_e^i$  as well) are all given (see Sec. II-B). Optimizing  $q^*$  and  $K_a$  at the same time leads to fairly a complicated NLP (nonlinear programming) problem, thus, here, we decompose it into two sub-problems and sequentially solve, first for  $(q^*, f_c^*, \tau_a^*)$  and then for  $K_a$ .

##### A. Nominal Configuration Optimization

The first sub-problem is to find  $q^*$  and its feasible  $(f_c^*, \tau_a^*)$  given the nominal task wrench  $f_e^*$  at the right hand. We formulate the following optimization problem for this:

$$\min_{q^*, f_c^*, \tau_a^*} f_1(q^*, f_c^*, \tau_a^*) \quad (33a)$$

$$\text{s.t. } \xi_c(q^*) \in \mathcal{X}_c, \xi_e(q^*) = \xi_e^d \quad (33b)$$

$$G(q^*) + J_c^T(q^*) f_c^* + \mathcal{S}_f K_f q_f^* = \mathcal{S}_a \tau_a^* + J_e^T(q^*) f_e^* \quad (33c)$$

$$f_c^* \in \mathcal{W}_c(q^*) \quad (33d)$$

$$\underline{q} < q^* < \bar{q} \quad (33e)$$

$$\underline{\tau}_a \leq \tau_a^* \leq \bar{\tau}_a \quad (33f)$$

where:

- The cost function in (33a) is designed as

$$\begin{aligned} f_1(q^*, f_c^*, \tau_a^*) &= w_1 \|\tau_a^*\|^2 + w_2 \|f_c^*\|^2 + w_3 \sum_{i=1}^n \sigma_i^2 (\bar{K}_{geo}^g(q^*) + \bar{K}_{geo}^e(q^*)) \end{aligned}$$

where the first term is to minimize the control effort  $\tau_a^*$ , and the second term to minimize the supporting contact wrench  $f_c^*$  while also reducing the the possibly-destabilizing  $\bar{K}_{geo}$  in (17) along with the third term minimizing  $\bar{K}_{geo}^g := \frac{\partial G(q)}{\partial q} |_{q^*}$  and  $\bar{K}_{geo}^e := \frac{\partial J_e^T(q) f_e^*}{\partial q} |_{q^*}$ . Here,  $w_1, w_2, w_3 > 0$  are some positive weights and  $\sigma_i$  is the  $i$ -th eigenvalue of a matrix.

- The constraints (33b) are to ensure that the right arm maintains the desired nominal pose  $\xi_e^d$  and the left arm keeps holding, or making contact with, the supporting surface  $\mathcal{X}_c$ .

- The constraint (33c) is to uphold the quasi-static equation (11) to generate  $f_e^*$  at the nominal equilibrium configuration  $q^*$ .
- The constraint (33d) is to enforce the supporting contact wrench constraint (6) or (7).
- The constraints (33e) and (33f) are just rewriting of the joint angle and torque limit constraints (8) and (9).

### B. Active Stiffness Optimization

Given  $(q^*, f_c^*, \tau_a^*)$  obtained from the first optimization sub-problem (33), here, we solve for  $K_a$  in (12) to ensure the system stability and the two inclusion constraints, (23) and (26), while utilizing  $K_f$  as much as possible. For this, we define the following optimization problem:

$$\min_{K_a} f_2(K_a) \quad (34a)$$

$$\bar{K}(K_a) > 0 \quad (34b)$$

$$\mathcal{W}_e^d \oplus \mathcal{B}_{\epsilon_1} \subset \bar{\mathcal{W}}_e^r(K_a) \quad (34c)$$

$$\mathcal{W}_e^d \oplus \mathcal{B}_{\epsilon_2} \subset \bar{\mathcal{W}}_e^c(K_a) \quad (34d)$$

$$\underline{K}_a \leq K_a \leq \bar{K}_a \quad (34e)$$

where:

- The cost function in (34a) is designed s.t.,

$$f_2(K_a) = \sum_{i=1}^{n_e} \sigma_i^2(K_e(K_a))$$

to minimize the task space stiffness  $K_e$  in (29) at the right arm end-effector to enhance its interaction compliance and robustness to disturbance, uncertainty, etc.

- The constraint (34b) is to enforce the positive-definiteness of  $\bar{K}$  even in the presence of possibly-destabilizing  $\bar{K}_{geo}$  in (16) and, consequently, the system stability.
- The constraints (34c) and (34d) are to enforce the two inclusion conditions (23) and (26), thereby, ensuring the feasibility of the solution to exert any  $f_e \in \mathcal{W}_e^d$  by the right arm under the joint torque limit constraint (9) and the supporting surface holding/contact constraint (i.e., (6) or (7)).
- The constraint (34e) is to ensure the well-behavedness of the solution  $K_a$  by enforcing it to be located between some lower bound  $\underline{K}_a$  and upper bound  $\bar{K}_a$ . We set each axis value of these  $\underline{K}_a$  and  $\bar{K}_a$  to be proportional to the joint torque limit.

It is worthwhile to mention that the stiffness analysis and the derived equations of Sec. III are particularly instrumental for the second optimization sub-problem (34). More precisely, if it were not for those analyses and derivations, we need to directly consider (15) with all  $(K_a, \delta q, \delta f_c) \in \mathbb{R}^{n_a \times n_a} \times \mathbb{R}^n \times \mathbb{R}^{n_c}$  being the optimization variables. In contrast, by using the various reduction equations of Sec. III, we only have  $K_a \in \mathbb{R}^{n_a \times n_a}$  as the search variables for the sub-problem (34). Further, using the affine presence of  $\delta f_e$  in  $\mathcal{W}_e^c$  (25) and in  $\mathcal{W}_e^r$  (22), the two inclusion constraints, (34c) and (34d), become rather straightforward to deal with. For instance, the  $\bar{\mathcal{W}}_e^r$ -inclusion constraint (34c) can be enforced simply by

$$\underline{\tau}_a \leq [A_\tau + B_\tau(K_a)\delta f_e^i] \oplus \mathcal{B}_{\epsilon_1} \leq \bar{\tau}_a, \quad \forall i \in \{1, 2, \dots, n_p\}$$

where  $\mathcal{B}_{\epsilon_1}$  is a ball of constant radius (i.e., independent from  $K_a$ ) conservatively estimated over the interval of  $K_a$  in (34e). Similarly, the  $\bar{\mathcal{W}}_e^c$ -inclusion constraint (34d) can be enforced simply by

$$[A_c + B_c(K_a)\delta f_e^i] \oplus \mathcal{B}_{\epsilon_2} \in \mathcal{W}_c, \quad \forall i \in \{1, 2, \dots, n_p\}$$

where, again,  $\mathcal{B}_{\epsilon_2}$  is a ball of radius independent from  $K_a$ . It is also equally worthy to recall that the stiffness analysis of Sec. III is crucial for the development of the feedback control  $\tau_a'$  at the interaction task wrench space of the right arm in Sec. IV. This stiffness analysis of Sec. III, to our knowledge, is explicitly revealed in this paper for the first time for the dual-arm robotic system on flexible base, and we believe it would also be applicable to other types of robots as well (e.g., Justin-DLR on flexible base [22]).

## VI. ROBUSTNESS AND STABILITY ANALYSIS

In this section, we analyze the robustness of our proposed framework in the presence of uncertainties, and also provide a formal proof of stability. Let us start with (1) with (2), which, with the uncertainty, can be written by

$$M(q)\ddot{q} + C(q, \dot{q})\dot{q} + G(q) + \mathcal{S}_f [B_f(q_f)\dot{q} + K_f(q_f)q] = \mathcal{S}_a \tau_a - J_c^T(q)f_c + J_e^T(q)f_e + \Delta \quad (35)$$

where  $\Delta \in \mathbb{R}^n$  contains such uncertainty effects as the modeling and parameter errors of the robot arms and the flexible base (e.g., friction), contact modeling error, etc. Here, we assume that  $\Delta$  is bounded, since, typically, this  $\Delta$  can become unboundedness only when  $\dot{q} \rightarrow \infty$  (e.g., all revolute joints with  $q_f, f_e, \tau_a$  bounded), which is prevented by the stability proof below with the bounded initial conditions  $(q, \dot{q})$  (i.e., if  $(q, \dot{q})$  and  $\Delta$  are initially bounded, they will be so thenceforth).

The quasi-static equation (4) also inherits this uncertainty  $\Delta$  s.t.,

$$G(q) + \mathcal{S}_f K_f q_f = \mathcal{S}_a \tau_a - J_c^T(q)f_c + J_e^T(q)f_e + \Delta$$

which can then in turn be perturbed around the nominal equilibrium configuration  $q^*$  (11) s.t.,

$$\bar{K}\delta q + J_c^T(q^*)\delta f_c = J_e^T(q^*)\delta f_e + \mathcal{S}_a \tau_a' + \Delta \quad (36)$$

where, with a slight abuse of notation,  $\Delta$  includes  $\Delta$  in (35) and also the remaining terms from the first-order Taylor's expansion of (14). Here, note that the nominal equilibrium  $q^*$  for the (perturbed) linear stiffness equation (36) is still the solution of (11) even in the presence of the uncertainty. This equation (11) will also be used for the configuration optimization in Sec. V-A (i.e., (33c)), although the constraints (34d) and (34e) will be made tighter with the uncertainty  $\Delta$  - see below.

Note also that, even with the uncertainty  $\Delta$ , the condition (18) should still be granted, since the penetration into the supporting surface  $\mathcal{X}_c$  is still zero. Then, similar to (19) and (20), we can obtain

$$\delta f_c = J_c^{\bar{K}+T}(q^*)[J_e^T(q^*)\delta f_e + \mathcal{S}_a \tau_a' + \Delta] \quad (37)$$

$$\bar{K}\delta q = N_c(q^*)[J_e^T(q^*)\delta f_e + \mathcal{S}_a \tau_a' + \Delta] \quad (38)$$



and, further, we can obtain the perturbed versions of (21) and (24) s.t.,

$$\tau_a = \tau_a^* - K_a S_a^T \bar{K}^{-1} N_c(q^*) [J_e^T(q^*) \delta f_e + S_a \tau_a' + \Delta] + \tau_a' \quad (39)$$

$$f_c = f_c^* + J_c^{\bar{K}+T} [J_e^T(q^*) \delta f_e + S_a \tau_a' + \Delta] \quad (40)$$

Here, note that  $(q^*, \tau_a^*, f_c^*)$  are given by the optimization of Sec. V, thus, all known. Injecting (39) into (22), we then have

$$\mathcal{W}_e^\tau := \{f_e \in \mathbb{R}^{n_e} \mid \tau_a \leq A_\tau + B_\tau \delta f_e + C_\tau \tau_a' + D_\tau \Delta \leq \bar{\tau}_a\}$$

implying that, to incorporate the uncertainty  $\Delta$ , the  $\bar{\mathcal{W}}_e^\tau$ -inclusion condition (23) should be modified s.t.,

$$\mathcal{W}_e^d \oplus \mathcal{B}_{\epsilon_1} \oplus \mathcal{B}_{\Delta_1} \subset \bar{\mathcal{W}}_e^\tau \quad (41)$$

where  $\mathcal{B}_{\Delta_1}$  denotes the bound of the perturbation  $D_\tau \Delta$ . On the other hand, injecting (40) into (25), we have

$$\mathcal{W}_e^c := \{f_e \in \mathbb{R}^{n_e} \mid A_c + B_c \delta f_e + C_c \tau_a' + D_c \Delta \in \mathcal{W}_c\}$$

resulting in the modification of the  $\bar{\mathcal{W}}_e^c$ -inclusion condition (26) by

$$\mathcal{W}_e^d \oplus \mathcal{B}_{\epsilon_2} \oplus \mathcal{B}_{\Delta_2} \subset \bar{\mathcal{W}}_e^c \quad (42)$$

where  $\mathcal{B}_{\Delta_2}$  is the ball of  $D_c \Delta$ . These perturbed inclusion conditions (41) and (42) should be used in the places of (34c) and (34d) in the optimization of Sec. V-B.

Of course, all these arguments stand upon the assumption that the system, even with the uncertainty, is stable (in the sense that all the states are bounded). To formally establish this stability, let us start with the feedback wrench control of Sec. IV. Then, applying (38) to (28), we can obtain

$$K_e \delta \xi_e = \delta f_e + S_e \tau_a' - S_\Delta \Delta \quad (43)$$

similar to (30) with  $S_\Delta := -K_e(q^*) J_e(q^*) \bar{K}^{-1} N_c(q^*)$ . Then, applying the feedback control  $\tau_a'$  in (31), similar to (32), the perturbed closed-loop dynamics can be obtained by

$$e_f + K_I \int_0^t e_f ds = S_\Delta \Delta \rightarrow e_f = \frac{s}{s + K_I} \mathcal{L}[S_\Delta \Delta]$$

where  $e_f := \delta f_e - \delta f_e^d$  and  $\mathcal{L}[\cdot]$  is the Laplace transform with  $s \in \mathbb{C}$  being the Laplace variable. This then implies that  $e_f, \int e_f ds$  are all bounded, and so is  $\tau_a'$  as well (with bounded  $\delta f_e^d$  and also  $\delta \xi_e$  (to be shown below)). Further, if  $K_I$  is large enough or  $\Delta$  is varying slow enough,  $e_f \approx 0$ .

Now, let us establish the stability of the total system. For this, by injecting  $\tau_a'$  (10) into (35) with (12) and also performing its first-order Taylor's expansion with  $q = q^* + \delta q$ ,  $\dot{q} = \frac{d}{dt} \delta q =: \delta \dot{q}$  and  $\ddot{q} = \frac{d^2}{dt^2} \delta q =: \delta \ddot{q}$  (with  $q^*$  being constant), we can have the linearized dynamics around  $q^*$  s.t.,

$$M(q^*) \delta \ddot{q} + \bar{B} \delta \dot{q} + \bar{K} \delta q = -J_c^T(q^*) \delta f_c + J_e^T(q^*) \delta f_e + S_a \tau_a' + \Delta' \quad (44)$$

where  $M(q^*)$ ,  $\bar{B} := S_f B_f S_f^T + S_a B_a S_a^T$  and  $\bar{K}$  are all symmetric and positive-definite ( $n \times n$ )-matrices, either from their construction (e.g.,  $M(q^*)$ ) or by our design (e.g., positive-definite/symmetric  $B_a$  for (12); enforcing (34b) for  $\bar{K}$ ). Further, 1)  $\Delta' := \Delta + \text{HOT}$  (i.e., Jacobian linearization error) is bounded around the equilibrium ( $\delta q, \delta \dot{q} = 0$ ); 2)  $\tau_a'$  is bounded

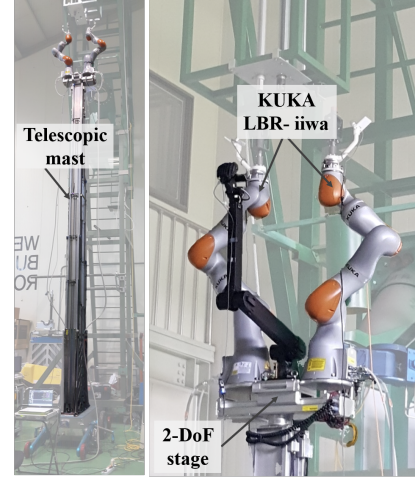


Fig. 6: Detailed description of the dual-arm telerobotic system for nuclear power plants. The flexibility of the telescopic mast is modeled by an elastic kinematic chain system with universal joints with torsional spring and damper

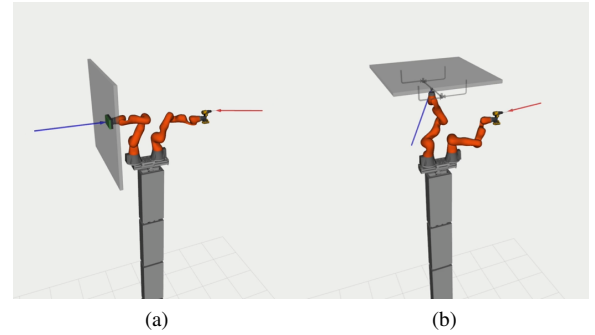


Fig. 7: Snapshots for the simulation with dual-arm telerobotic system in Fig. 6: (a) Snapshot for the force tracking simulation with frictional contact. (b) Snapshot for the force tracking simulation with holding support.

as stated above; and 3)  $\delta f_c$  and  $\delta f_e$  are also bounded, since they are produced by  $\tau_a$ , which is in turn bounded since, in (39),  $\tau_a^*, \delta f_e, \tau_a', \Delta$  are all bounded. This then establishes the stability of the total system, since the dynamics on the left-hand side of (44) is linear time-invariant and Hurwitz, while the disturbances on its right-hand side are all bounded.

## VII. EVALUATION

In this section, we present the evaluation results to validate the efficacy of the proposed control framework through extensive simulations and experiments. The evaluation involves two types of the dual-arm robot system on the flexible base; 1) simulations on the dual-arm telerobotic system for a nuclear power plant in Fig. 1b [2], [3], 2) simulations and experiments on the dual-arm franka system on the 4-DoF flexible base.

### A. Simulation on Dual-Arm Telerobotic System for Nuclear Power Plant

1) *System Setup*: We first perform simulations on the dual-arm telerobotic system for height operations in the nuclear

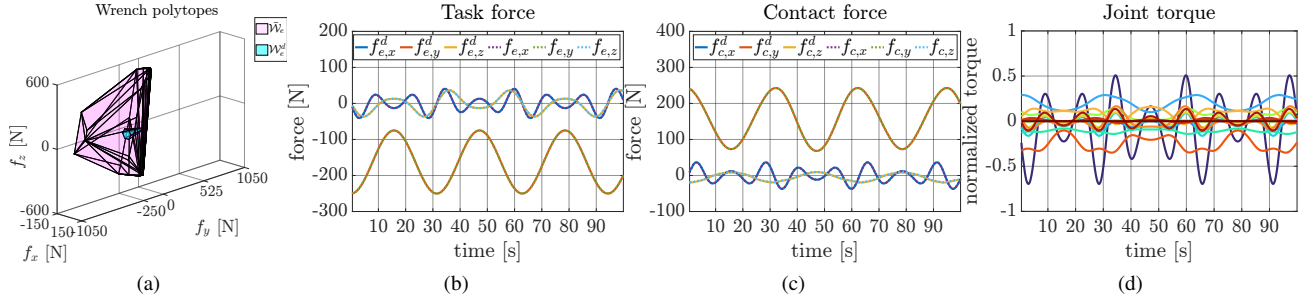


Fig. 8: Simulation results for the force tracking with the frictional contact (a) Wrench polytope generation result. (b) Task force tracking result. (c) Contact force. (d) Normalized joint torque actuation.

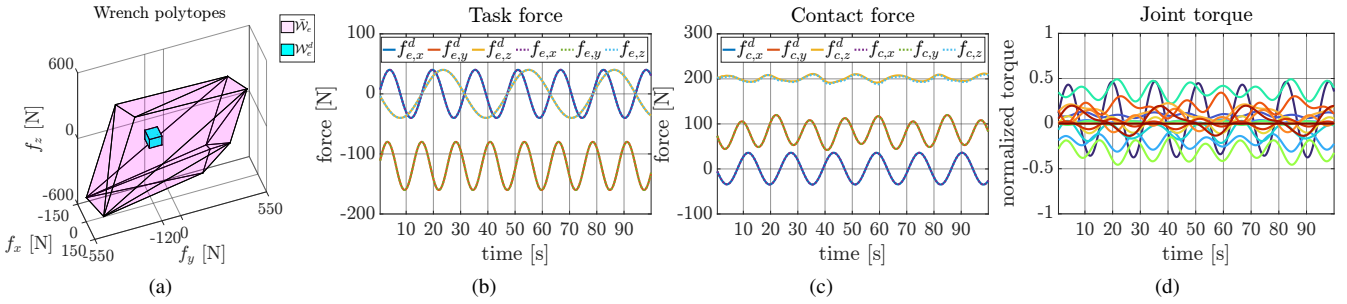


Fig. 9: Simulation results for the force tracking with the bilateral holding contact (a) Wrench polytope generation result. (b) Task force tracking result. (c) Contact force. (d) Normalized joint torque actuation.

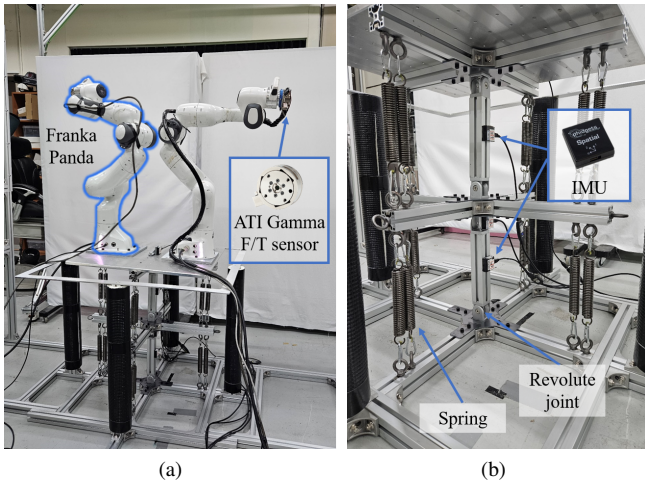


Fig. 10: (a) System setup of the dual-arm franka system on the 4-DoF flexible base. (b) Detail of the flexible base with IMU sensor attachment.

power plant in Fig. 1b [2], [3]. The detailed description of the dual-arm telerobotic system setup is shown in Fig. 6. The system consists of two 7-DoF KUKA-LBR-iiwa R820 manipulators, a 2-DOF actuated stage system, and a telescopic mast with a fixed mobile base. The telescopic mast exhibits the flexibility induced by the assembly tolerance among each adjacent segment of the telescopic structure. Following this, we model the dynamics of the mast as a 12-DoF elastic kinematic chain (EKC) system [49] where each segment is connected via a 2-DOF universal joint, and the flexibility of

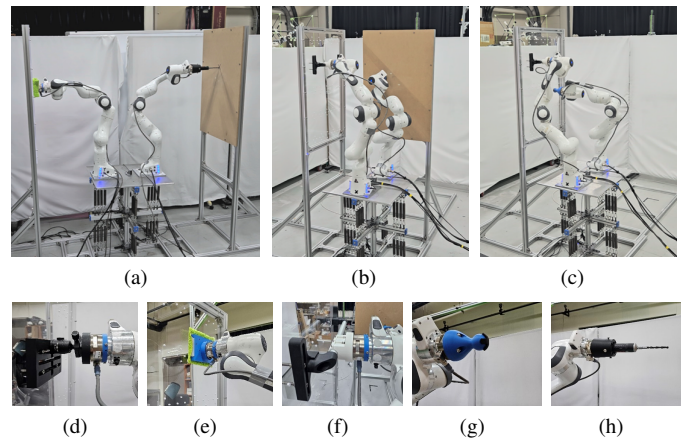


Fig. 11: Environmental setup and the tool setup for the dual-arm franka system on the 4-DoF flexible base. (a) Environment with parallel task wall and the contact wall. (b) Environment with task wall and the contact wall in  $90^\circ$ . (c) Environment with task wall and the contact wall in the same direction. (d) Spherical joint tool attached to the left arm for bilateral holding. (e) flat contact tool attached to the left arm for frictional contact. (f) Pipe grasping tool attached to the left arm. (g) Spherical tooltip attached to the right arm for the wrench execution. (g) Drilling tool attached to the right arm for the drilling task.

the mast can be modeled as a torsional spring and damper equipped at each joint.

2) *Result*: For the simulation, two control scenarios are considered to validate the performance of the proposed control

Optimization Results: Bilateral Holding						
#	Task			Results		
	$p_e^d$ (m)	$f_e^*$ (N)	$\delta f_e^i$ (N)	Time (s)	$p_c$ (m)	$\text{vec}(K_a^*)$ (N·m/rad)
I	[0.8;0.0;1.6]	[0;0;0]	[35;35;28], [35;35;-28], [35;-35;28], [35;-35;-28], [-35;35;28], [-35;35;-28], [-35;-35;28], [-35;-35;-28]	46.44	[-0.7;-0.04;1.54]	[228.48, 207.71, 181.83, 171.66, 101.39, 55, 50, 308.17, 200, 150.99, 127.27, 124.79, 113.44, 101.81]
II	[0.85;-0.05;1.6]	[-30;0;0]	[20;30;30], [20;30;-30], [20;-30;30], [20;-30;-30], [-30;30;30], [-20;30;-30], [-20;-30;30], [-20;-30;-30]	127.22	[-0.7;-0.15;1.5]	[977.38, 906.68, 574, 531.08, 100, 50.00, 50.70, 219.46, 200, 206.87, 213.12, 206.47, 144.65, 145.58]
III	[1.0;-0.05;1.5]	[-10;0;0]	[0;0;0], [-40;5;8.66], [-40;-5;8.66], [-40;5;-8.66], [-40;-5;-8.66], [-40;10;0], [-40;-10;0]	19.10	[-0.7;-0.09;1.5]	[220, 200, 121, 110, 100, 55, 50, 220, 200, 121, 110, 100, 55, 50]

TABLE I: Optimization results for the case of bilateral holding

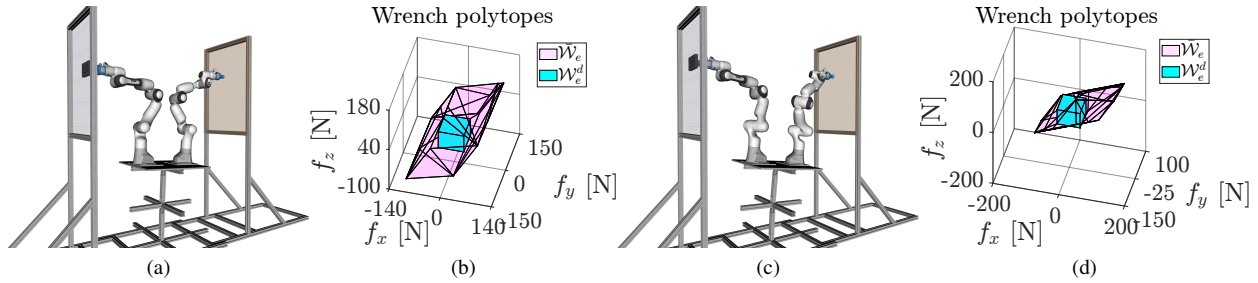


Fig. 12: Comparison between the optimized solution and the unoptimized variables in the case of the bilateral holding. (a) Visualization of the optimized configuration. (b) Wrench polytope generation result from the optimized solution. (c) Visualization of the unoptimized configuration. (d) Wrench polytope generation result from the unoptimized variables.

framework. The first scenario is to perform force tracking with the frictional contact to the vertical wall in a parallel direction, and the second scenario is to perform desired force tracking with another type of  $\mathcal{W}_e^d$  with the bilateral holding to the horizontal wall above the system as shown in Fig. 7. Both scenarios execute the 3-DoF desired task force ( $n_e = 3$ ) while maintaining 3-DoF supporting contact ( $n_c = 3$ ). Simulation results in Fig. 8 and Fig. 9 show the simulation results including wrench polytope generation result, task force comparison between  $f_e$  and  $f_e^d$ , contact force comparison between  $f_c$  and  $f_c^d$  calculated by (24), and the normalized joint torque  $\frac{\tau_i}{\tau_i^{lim}}$ , which verify the efficacy of the proposed control framework.

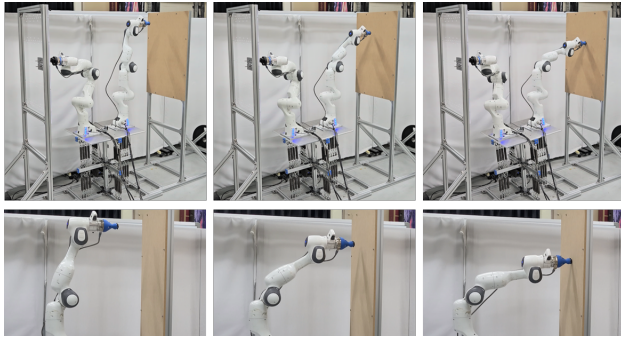
### B. Experiment on Dual-Arm Franka System on 4-DoF Flexible Base

1) *System Setup*: Next, we perform extensive experiments on the dual-arm franka system on a 4-DoF flexible base in Fig. 10, which mimics the system in Fig. 6. The system consists of a 7-DoF Franka Panda manipulator (3kg payload for each arm) with the 1kHz control rate, and a flexible base with a 4-DoF ( $n_f = 4$ ) EKC modeling with a universal joint connection which comes from the telescopic mast modeling in Fig. 6. For the base flexibility, linear springs are mounted between each segment as shown in Fig. 10b, and we can approximate the stiffness model of this spring attachment as a joint spring model, which can be linearized near the equilibrium point. ATI-Gamma 6-axis F/T sensor is attached to the end-effector of each arm for the contact wrench and the task wrench measurement. For the base state estimation,

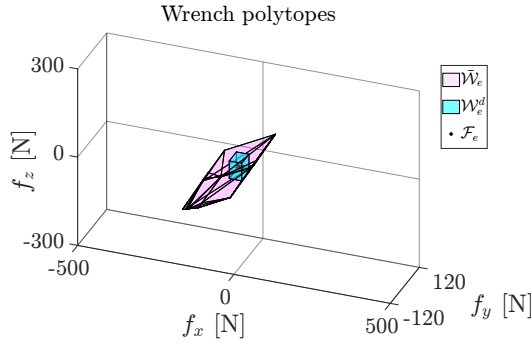
inertial measurement unit (IMU) sensors (PhidgetSpatial 0/0/3 Basic model) are attached to each link of the base with a 250Hz measurement rate.

The experimental results include two cases of the environmental setup. First, the system is equipped with the mock-up environment which consists of the left wall for the supporting contact and the right wall for the task execution in parallel with each other as described in Fig. 11a. Two types of supporting contact are adopted as described in Sec. II-B; the bilateral holding as in (6) and the frictional contact as in (7). We set  $n_c = 3$  for both contact types such that only contact force is considered. Also, the boundedness of the bilateral holding is  $\alpha = 70$  N, and the friction coefficient is  $\mu = 0.3$ . Two equivalent contact tools are equipped at the left arm for each contact type; a spherical joint tool setup for the bilateral holding as shown in Fig. 11d and a flat contact tool for the frictional contact as shown in Fig. 11e.

The experiment for parallel environments includes three scenarios. First, we compare the wrench polytope generation results to check the task wrench feasibility. For given target task information, we compare the generated polytopes  $\mathcal{W}_e^c$  and  $\mathcal{W}_e^d$  to check whether these polytopes cover  $\mathcal{W}_e^d$  for the optimized solution in (33)-(34) and for the unoptimized variables. The unoptimized variables are set to only satisfying (33b)-(33c) and (33e)-(33f). For the second scenario, we aim to check the feedback wrench control performance. The system is required to execute desired task wrench  $f_e^d \in \mathcal{W}_e^d$  to the right wall. The third scenario is to perform a drilling task for the practical task validation. The system is required to make a hole in the right wall with the drilling tool by executing the



(a)



(b)

Fig. 13: (a) Snapshots for the force tracking experiment with bilateral holding. (b) Wrench polytope generation result.

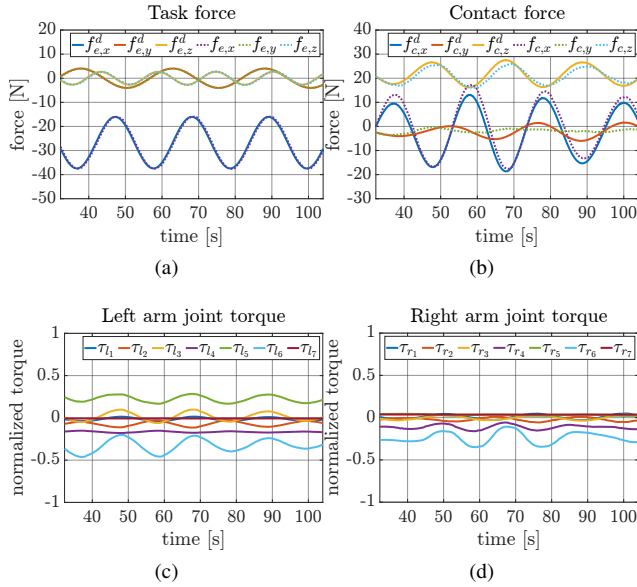
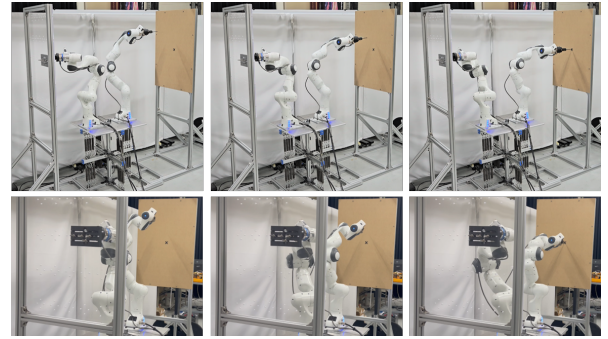
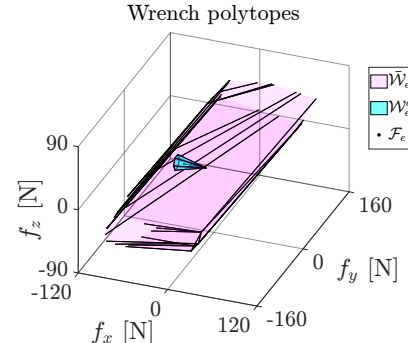


Fig. 14: Experimental results for the force tracking with bilateral holding. (a) Task force tracking result. (b) Contact force. (c) Normalized left arm joint torque. (d) Normalized right arm joint torque.

desired drilling force. These scenarios are performed for each contact type. We set  $n_e = 3$  during the validation such that only task force is considered. Also, there are two types of tools that are equipped at the right arm for each scenario; a spherical tooltip for the second scenario as shown in Fig. 11g and an automatic drilling tool (Bosch Go) for the third scenario as shown in Fig. 11h.



(a)



(b)

Fig. 15: (a) Snapshots of the drilling task with bilateral holding. (b) Wrench polytope generation result.

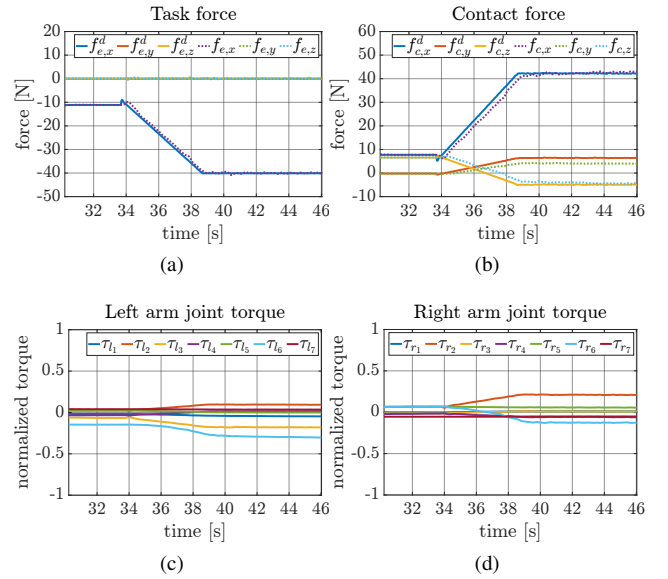


Fig. 16: Experimental results for the drilling task with bilateral holding. (a) Task force tracking result. (b) Contact force. (c) Normalized left arm joint torque. (d) Normalized right arm joint torque.

The second environmental setup case is to equip the system at the mock-up environment which consists of the contact wall and the task wall in a non-parallel direction with each other. The wall for the supporting contact is equipped in  $90^\circ$  as shown in Fig. 11b or equipped in the same direction as shown in Fig. 11c. The system is required to execute the desired task wrench to the task wall for each environmental setup. The spherical tooltip in Fig. 11g is equipped at the right arm to

Optimization Results: Frictional Contact						
Task				Results		
#	$p_e^d$ (m)	$f_e^*$ (N)	$\delta f_e^z$ (N)	Time (s)	$p_c$ (m)	$\text{vec}(K_a^*)$ (N-m/rad)
I	[0.8;0.0;1.6]	[0;0;0]	[0;0;0], [-40;5;8.66], [-40;-5;8.66], [-40;5;-8.66], [-40;-5;-8.66], [-40;10;0], [-40;-10;0]	28.76	[-0.7;0.17;1.48]	[336.33, 305.76, 277.96, 252.69, 229.72, 208.84, 89.00, 1000, 627.77, 121, 110, 100, 55, 50]
II	[0.85;-0.05;1.55]	[-10;0;0]	[0;0;0], [-30;7.5;13], [-30;-7.5;13], [-40;7.5;-13], [-30;-7.5;-13], [-30;15;0], [-30;-15;0]	36.15	[-0.7;-0.08;1.72]	[323.09, 293.72, 121, 110, 100, 55, 50, 231.58, 210.52, 121, 110, 100, 55, 50]
III	[1.0;0.0;1.6]	[-10;0;0]	[0;0;0], [-40;3;5.20], [-40;-3;5.20], [-40;3;-5.20], [-40;-3;-5.20], [-40;6;0], [-40;-6;0]	23.58	[-0.7;-0.06;1.54]	[220, 200, 121, 110, 100, 55, 50, 220, 200, 121, 110, 100, 55, 50]

TABLE II: Optimization results for the case of the frictional contact

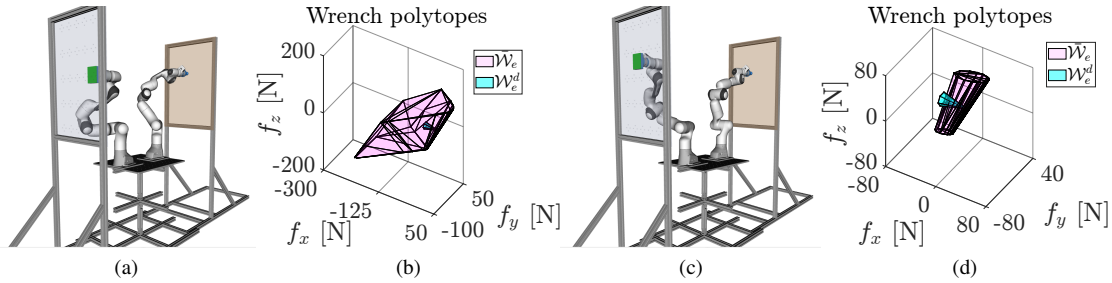


Fig. 17: Comparison between the optimized solution and the unoptimized variables in the case of the frictional contact. (a) Visualization of the optimized configuration. (b) Generated wrench polytopes from the optimized solution. (c) Visualization of the unoptimized configuration. (d) Generated wrench polytopes from the unoptimized variables.

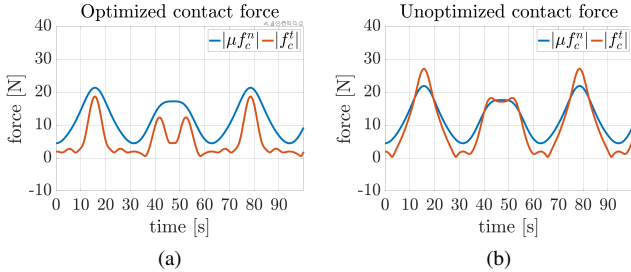


Fig. 18: Contact force comparison between the optimized solution and the unoptimized variables in the case of the frictional contact. The friction cone constraint is violated such that slip occurs for the unoptimized case.

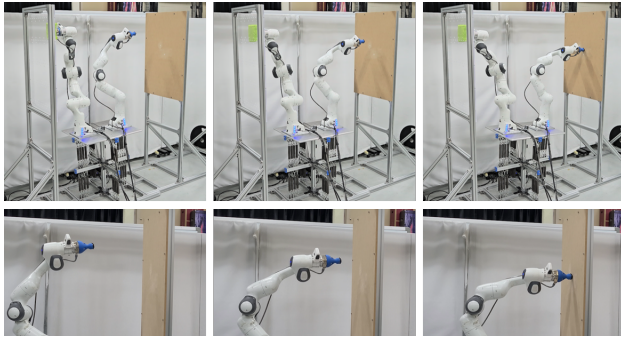
perform the wrench execution, and the left arm is holding the left wall pipe during the task as shown in Fig. 11f.

In addition to extensive experimental validation scenarios, we additionally perform a 6-DoF wrench tracking simulation to verify the capability of 6-DoF wrench execution of the proposed control framework. The simulation is performed in the parallel environment setup with the bilateral holding contract.

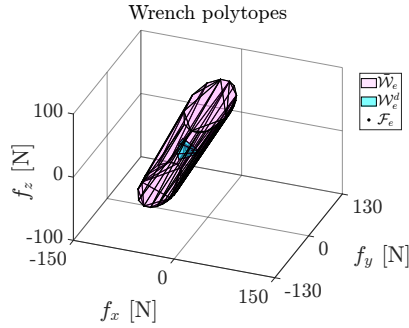
To evaluate the control performance across each experimental and simulation scenario, we present the comparison between the measured and desired wrenches (task force  $f_e$  vs.  $f_e^d$ , contact force  $f_c$  vs.  $f_c^d$  as defined in (24)), the normalized joint torques  $\frac{\tau}{\tau_{lim}}$ , and pose error results (for both task and contact poses). Additionally, the NLOpt [50] optimization library is employed to solve the proposed optimization framework in Sec. V. NLOpt supports nonlinear optimization

problems with nonlinear constraints, and in this paper, we utilize the COBYLA solver option within the library.

2) *Result - parallel environment case*: Table. I shows the information of target tasks and optimization results for the validation of the bilateral holding including supporting contact position calculated from  $q^*$ , calculation time, and  $K_a^*$ . We restrict  $K_a^*$  to a diagonal matrix during the validation, and this can be easily extended for non-diagonal  $K_a^*$  cases. The result for the scenario I is shown in Fig. 12. We can see that the generated  $\mathcal{W}_e$  from the optimization solution can cover  $\mathcal{W}_e^d$  as shown in Fig. 12b, while the  $\mathcal{W}_e$  cannot cover the  $\mathcal{W}_e^d$  such that we cannot ensure the joint torque limit and contact wrench constraints during the task for the case of unoptimized variables as shown in Fig. 12d. The result for scenario II of validating the feedback wrench control performance is shown in Fig. 13 with its forces and control actuation measurement results in Fig. 14. As shown in Fig. 13b,  $\mathcal{W}_e^d$  is covered by  $\mathcal{W}_e$  such that the optimized solution ensures the task wrench feasibility. Also, from the task force tracking result in Fig. 14a (RMS error: [0.60;0.12;0.18] (N)) and the contact force comparison result in Fig. 14b (RMS error: [2.66;2.03;1.37] (N)), we can validate the performance of the feedback wrench control with the maximum 37.77 N task wrench execution. The task position (RMS error: [0.006; 0.006; 0.003] (m)) and the supporting contact position (RMS error: [0.007; 0.009; 0.022] (m)) results validate the precise task execution of the system. For scenario III of the drilling task, the system is required to execute linearly increasing drilling force with 40N saturation in the task wall's normal direction. The result is shown in Fig. 15 with its forces and control actuation measurement results in Fig. 16. The system can successfully perform the



(a)



(b)

Fig. 19: (a) Snapshots for the force tracking experiment with frictional contact. (b) Wrench polytope generation result.

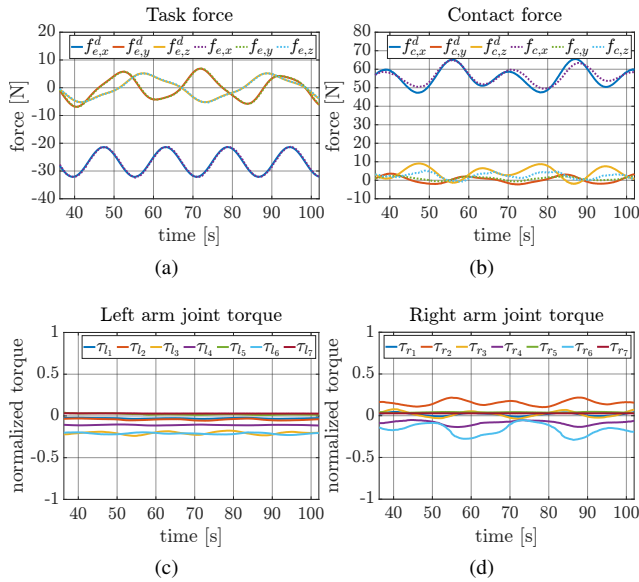
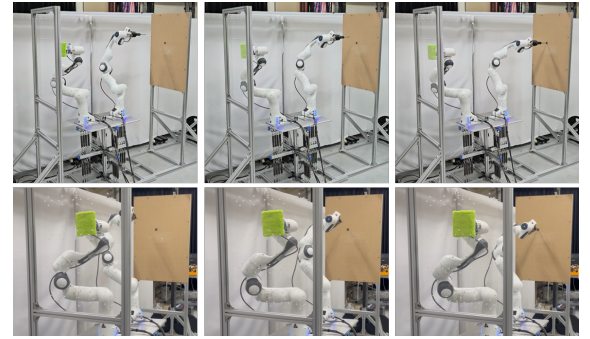
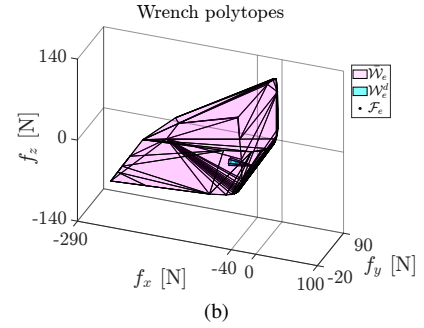


Fig. 20: Experimental results for the force tracking experiment with frictional contact. (a) Task force tracking result. (b) Contact force. (c) Normalized left arm joint torque. (d) Normalized right arm joint torque.

drilling task and make a hole at the right wall as shown in Fig. 15a. As shown in Fig. 15b, the optimized solution ensures the task wrench feasibility. The task force tracking result is shown in Fig. 16a (RMS error: [0.73;0.06;0.16] (N)) and the contact force comparison result is shown in Fig. 16b (RMS error: [1.56;1.78;1.18] (N)) with the maximum 40.81 N task wrench execution. Also, the system precisely follows



(a)



(b)

Fig. 21: (a) Snapshots for the drilling experiment with frictional contact. (b) Wrench polytope generation result.

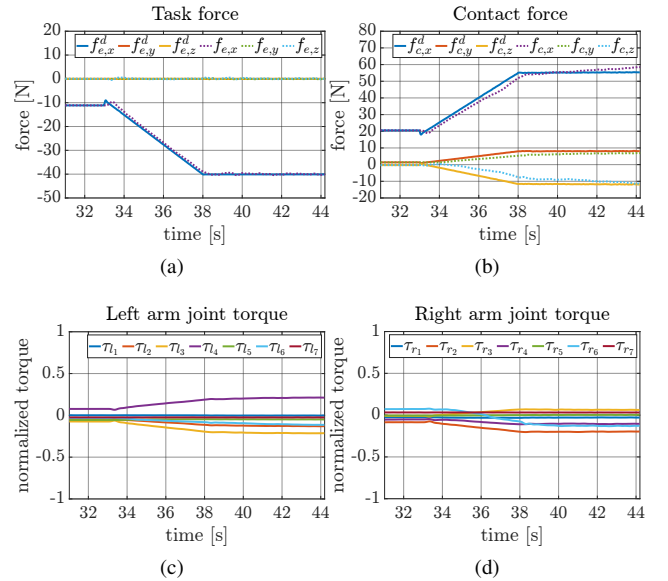


Fig. 22: Experimental results for the drilling task with frictional contact. (a) Task force tracking result. (b) Contact force. (c) Normalized left arm joint torque. (d) Normalized right arm joint torque.

the desired position (task position RMS error: [0.006; 0.022; 0.007] (m), supporting contact position RMS error: [0.009; 0.005; 0.006] (m)).

Table. II shows the information of target tasks and optimization results for the validation with frictional contact including contact position calculated from  $q^*$ , calculation time, and  $K_a^*$  as same with Table. I, and we also restrict  $K_a$  to diagonal stiffness during the point contact task scenarios. Considering the unilateral property of the frictional contact, we set  $\mathcal{W}_e^d$  as

Optimization Results: Non-parallel Environment						
Case	Task			Results		
	$p_e^d$ (m)	$f_e^*$ (N)	$\delta f_e^*$ (N)	Time (s)	$p_c$ (m)	$\text{vec}(K_\alpha^*)$ (N·m/rad)
90° wall	[0.7; 0.1; 1.55]	[0;0;0]	[0;0;0], [-60;5;8.66], [-60;-5;8.66], [-60;5;-8.66], [-60;-5;-8.66], [-60;10;0], [-60;-10;0]	37.11	[-0.075, 0.4, 1.7]	[367.52, 378.32, 455.52, 471.86, 291.37, 50, 127.90, 362.75, 229.51, 100, 202.51, 229.00, 119.14, 124.88]
Same wall	[0.15; 0.465; 1.4]	[0;0;0]	[10;50;10], [10;-50;10], [10;50;-10], [10;-50;-10], [-10;50;10], [-10;-50;10], [-10;50;-10], [-10;-50;-10]	84.38	[-0.093, 0.4, 1.7]	[220, 200, 121, 110, 100, 55, 50, 220, 200, 121, 110, 100, 55, 50]

TABLE III: Optimization results for the non-parallel environment setup.

a cone-type polytope with dominant task wall normal force. First, the result for scenario I is shown in Fig. 17. We can see that the generated  $\mathcal{W}_e$  from the optimization solution can cover  $\mathcal{W}_e^d$  as shown in Fig. 17b, while  $\mathcal{W}_e$  cannot cover the  $\mathcal{W}_e^d$  as shown in Fig. 17d such that the friction cone constraint is violated and the sliding occurs in the case of the unoptimized case (see Fig. 18 which compare  $\mu f_c^n$  and  $f_c^t$ ). The result for scenario II of validating the feedback wrench control performance is shown in Fig. 19 with its forces and control actuation measurement results in Fig. 20. The result of generated wrench polytopes by the optimization in Fig. 19b shows the guarantee of the task wrench feasibility. The task force tracking result is shown in Fig. 20a (RMS error: [1.97; 1.13; 2.76] (N)) and the contact force comparison result is shown in Fig. 20b (RMS error: [1.97; 1.13; 2.76] (N)) with the maximum 33.21 N task wrench execution. Also, the system precisely follows the desired position (task position RMS error: [0.003; 0.008; 0.013] (m)), supporting contact position RMS error: [0.006; 0.020; 0.007] (m)). The result for scenario III of the drilling task is shown in Fig. 21 with its forces and control actuation measurement results in Fig. 22. Similar to the bilateral holding case, the system can successfully perform the drilling task and make a hole at the right wall as shown in Fig. 21a and the wrench polytope generation result in Fig. 15b ensures the task wrench feasibility. The task force tracking result is shown in Fig. 22a (RMS error: [0.70; 0.06; 0.19] (N)) and the contact force comparison result is shown in Fig. 22b (RMS error: [1.96; 1.56; 2.76] (N)) with the maximum 40.45 N task wrench execution. Also, the system precisely follows the desired position (task position RMS error: [0.007; 0.005; 0.007] (m)), supporting contact position RMS error: [0.003; 0.027; 0.010] (m)).

3) *Result - non-parallel environment case*: Table. III shows the information of the target task for each environmental setup, and the system is required to execute the desired task wrench. First, the force tracking result for the 90° environment setup is shown in Fig. 23 with its forces and control actuation measurement results in Fig. 24. The result of generated wrench polytopes by the optimization in Fig. 23b shows the guarantee of the task wrench feasibility. The task force tracking result is shown in Fig. 24b (RMS error: [0.50; 0.12; 0.12] (N)) and the contact force comparison result is shown in Fig. 24a (RMS error: [1.59; 0.72; 2.27] (N)) with the maximum 43.28 N task wrench execution. The task position result shows [0.012; 0.039; 0.005] (m) RMS error and the supporting contact position result shows [0.019; 0.058; 0.008] (m) RMS error.

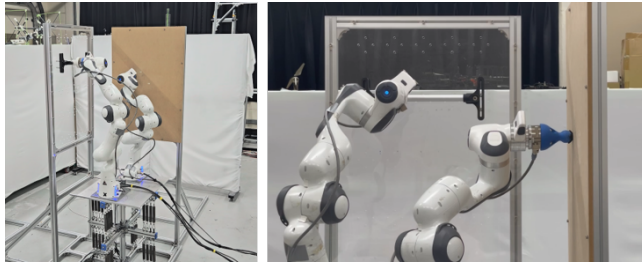
In the same way, the force tracking result for the same direction environment setup is shown in Fig. 25 with its forces and control actuation measurement results in Fig. 26. The result of generated wrench polytopes by the optimization in Fig. 25b shows the guarantee of the task wrench feasibility. The task force tracking result is shown in Fig. 26b (RMS error: [0.22; 0.45; 0.16] (N)) and the contact force comparison result is shown in Fig. 26a (RMS error: [1.10; 0.93; 0.91] (N)) with the maximum 43.43 N task wrench execution. The task position result shows [0.006; 0.055; 0.042] (m) RMS error and the supporting contact position result shows [0.010; 0.074; 0.007] (m) RMS error.

4) *Result - 6-DoF wrench simulation*: Table. IV shows the information of the target task, and the system is required to execute the 6-DoF desired task wrench in the parallel environmental setup. The simulation results are shown in Fig. 27 and Fig. 28, which shows the capability of the 6-DoF full wrench execution of the proposed control framework.

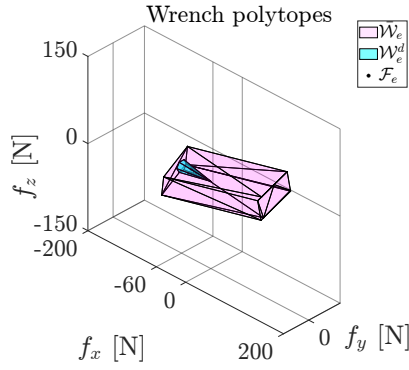
## VIII. DISCUSSION

In Sec. VII, extensive simulations and experiments were performed to demonstrate the efficacy of the proposed framework, showing its ability to handle high-force/high-precision tasks by utilizing supporting contact. The results indicate that the proposed control framework effectively addresses the challenges posed by base flexibility. Specifically, the utilization of the supporting surface allows for stable task execution by mitigating the oscillations and deformations that typically arise in flexible bases. This can be clearly observed in Fig. 29, which compares the base joint motion measurements between tasks executed with and without the utilization of the supporting surface. The experimental data further demonstrate the system's wrench capability, exceeding the payload limit of a single robot arm on a flexible base (3kg payload for the Franka Emika Panda), and showing its ability of precise force tracking (task force RMS error avg: 1.12 N, std: 1.20 N, contact force RMS error avg: 3.02 N, std: 0.78 N) and the pose (task and contact) regulation (task pose RMS error avg: 0.028 m, std: 0.023 m, contact pose RMS error avg: 0.037 m, std: 0.025 m) during demanding operations. We believe that the proposed control framework would also be applicable to other types of robotic platforms.

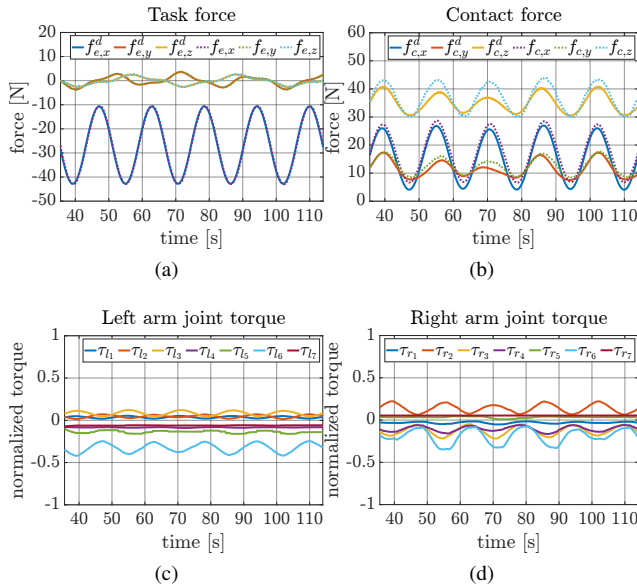
Our control framework, while effective in many scenarios, still presents some limitations to be considered. First, we observed a larger error in contact force tracking results compared to the task force tracking results. This discrepancy is likely due



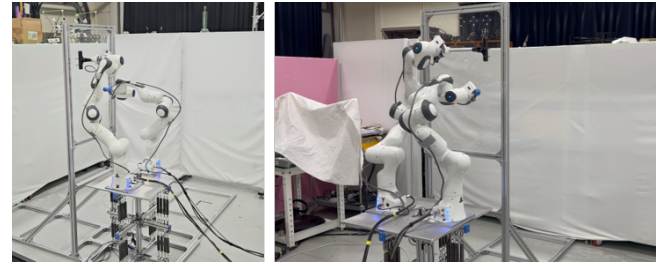
(a)



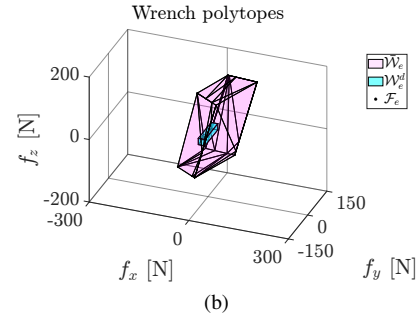
(b)

 Fig. 23: (a) Snapshots for the force tracking experiment with  $90^\circ$  direction environment setup. (b) Wrench polytope generation result.

 Fig. 24: Experimental results for the force tracking experiment with  $90^\circ$  direction environment setup. (a) Task force tracking result. (b) Contact force. (c) Normalized left arm joint torque. (d) Normalized right arm joint torque.

to some factors including modeling inaccuracies (e.g., dynamics modeling, friction/contact modeling) and environmental kinematic errors. Although the proposed control framework ensures robustness and stability under these uncertainties as discussed in Sec. VI, these factors can still lead to deviations in contact force tracking. While the task force error can be mitigated by the PI control strategy of  $\tau'_a$  in (31), the absence of specific feedback control for the contact force results in



(a)



(b)

Fig. 25: (a) Snapshots for the force tracking experiment with same direction environment setup. (b) Wrench polytope generation result.

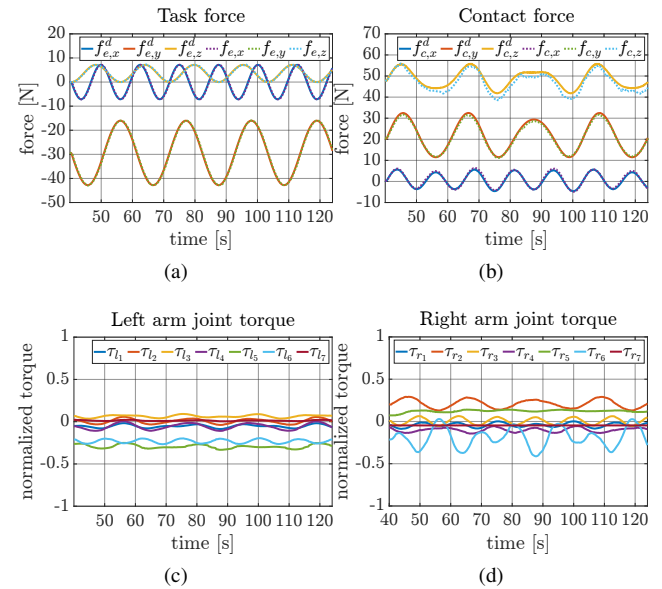


Fig. 26: Experimental results for the force tracking experiment with same direction environment setup. (a) Task force tracking result. (b) Contact force. (c) Normalized left arm joint torque. (d) Normalized right arm joint torque.

higher tracking errors.

Also, while the proposed approach relies on the quasi-static stiffness analysis and is effective for near-nominal configuration behavior, may not fully capture the dynamic behaviors of the system, such as the varying environmental conditions or under substantial system motions. This reliance could lead to discrepancies between the predicted and actual system behavior, leading to inconsistencies such as the aforementioned contact force errors and stiffness variability during substantial motion.

Another limitation arises from the geometric stiffness  $K_{geo}$ .



Optimization Results: 6-DoF Wrench Tracking						
Task				Results		
Case	$p_e^d$ (m)	$f_e^*$ (N·m, N)	$\delta f_e^i$ (N·m, N)	Time (s)	$p_c$ (m)	$\text{vec}(K_a^*)$ (N·m/rad)
I	[0.8; 0.0; 1.6]	[0;0;0;0;0;0]	[±5;±1.1;±1.1;±10;±17;±17]	48.03	[-0.07;0.11;1.5]	[220, 200, 121, 110, 100, 55, 50, 220, 200, 121, 110, 100, 55, 50]

TABLE IV: Optimization results for the 6-DoF wrench tracking simulation.

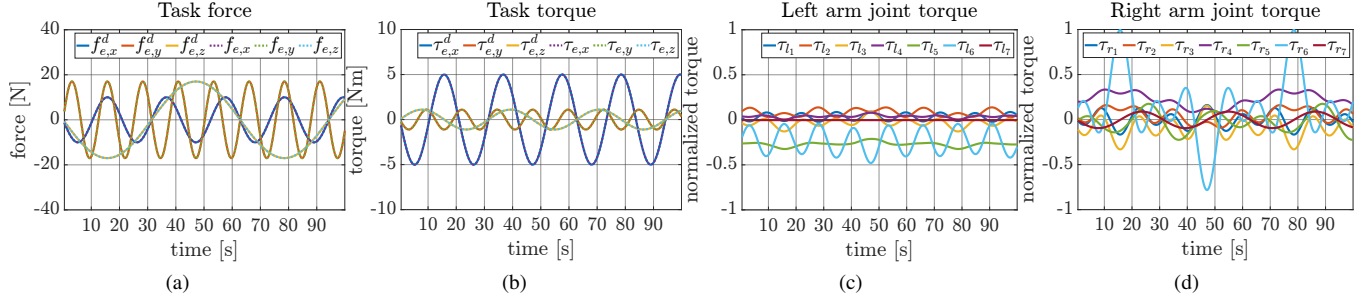


Fig. 27: Simulation results for the force tracking with the frictional contact (a) Wrench polytope generation result. (b) Task force tracking result. (c) Contact force. (d) Normalized joint torque actuation.

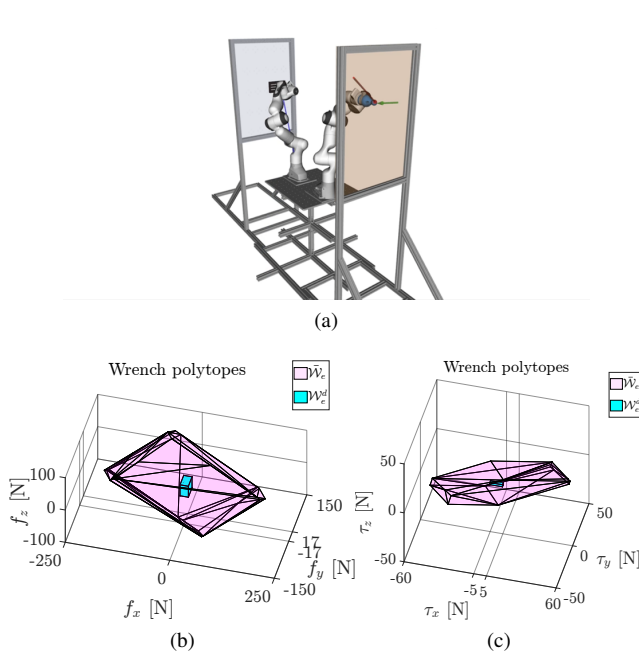


Fig. 28: (a) Snapshot for the 6-DoF wrench tracking simulation. The red arrow represents the task force, and the green arrow represents the task torque. (b) Force polytope generation result. (c) Torque polytope generation result.

While the simulation and experimental results show that the potential instability of  $K_{geo}$  can be mitigated by properly designed base stiffness  $K_f$  and the optimized active stiffness  $K_a$  in practice, it is theoretically possible that the optimization may fail to calculate feasible  $K_{geo}$ , potentially leading to instability. Although system damping may partially address this instability, we have not yet addressed the rigorous analysis for such instability conditions.

Finally, there are possible improvements to be made in the optimization process regarding adaptation and computational efficiency. The proposed sequential optimization framework

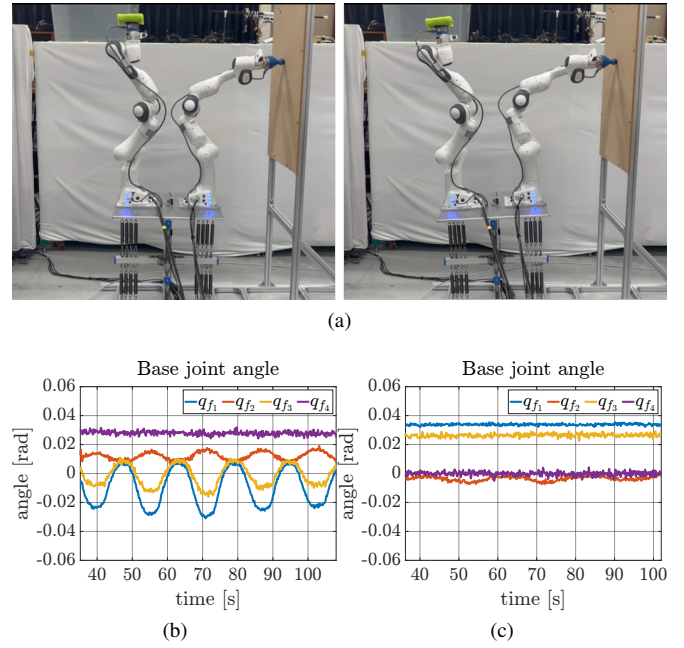


Fig. 29: (a) Snapshot for the task force execution without supporting contact. The flexible base (b) The base joint motion during the task force execution without supporting contact. (c) The base joint motion during the task force execution utilizing supporting contact (scenario II for the frictional contact with parallel wall environment),

identifies optimal solutions effectively in an offline manner, based on pre-determined information. However, it may yield infeasible solutions under certain conditions, such as when the supporting surface is improperly positioned or when environmental constraints are particularly stringent, which require adaptation strategies to handle this issue. Moreover, the framework may not be well-suited for real-time adaptation in unexpected situations due to computational limitations, especially during sudden changes in task environments, contact conditions, or external disturbances (e.g., impact or vibration).

To address these limitations, our research directions for the future work include:

- Extension of the proposed control framework to the other types of robot platforms (e.g., humanoid, quadrupeds) with various types of contact (e.g., single and multi-contact).
- Robust optimization and adaptive control considering uncertainties.
- Rigorous dynamics analysis and control strategy for the operation with substantial and/or dynamic motion (e.g. contact transition, hybrid motion-force control).
- Rigorous stability analysis of geometric stiffness.
- Adaptation strategy and computational improvements in the optimization framework.

## IX. CONCLUSION

In this paper, we propose a novel high-force/high-precision interaction control framework of a dual-arm robot system on a flexible base by utilizing the supporting surface with one arm. Based on the integrated control design, which encompasses nominal control, stiffness control, and feedback wrench control, our framework optimizes the nominal configuration (with its related wrenches) and the active stiffness control gain to achieve the target interaction task. Also, by introducing novel stiffness analysis with system flexibility, we can obtain a peculiar linear relation among contact wrench, task wrench, and active control such that we can simplify the optimization process and facilitate the feedback wrench control design. The stability and the robustness are also analyzed under uncertainties, and we present some simulation and experimental results to validate the efficacy of the proposed control framework.

## REFERENCES

- [1] H. Shin, S. H. Jung, Y. R. Choi, B. Choi, and C. Kim, "Development of a shared remote control robot for aerial work in nuclear power plants," *Nuclear Engineering and Technology*, vol. 50, no. 4, pp. 613–618, 2018.
- [2] C. Ha, H. Kim, and D. Lee, "Passivity-based control of manipulator-stage systems on vertical flexible beam," in *Proc. IEEE/RSJ Int'l Conference on Intelligent Robots and Systems*, 2017, pp. 429–435.
- [3] H. Kim, C. Ha, J. Ahn, J. Lee, and D. Lee, "User interface design for semi-autonomous teleoperation of manipulator-stage system on flexible beam," in *In IEEE 2018 15th International Conference on Ubiquitous Robots (UR)*, 2018, pp. 96–102.
- [4] M. OSUMI. (2022) Very big tech enlisted to tackle risky railway tasks in japan. [Online]. Available: <https://www.japantimes.co.jp/news/2022/05/02/business/tech/jr-west-robots-safety/>
- [5] J. Feng and W. Zhang, "Autonomous live-line maintenance robot for a 10 kv overhead line," *IEEE Access*, vol. 9, pp. 61 819–61 831, 2021.
- [6] M. R. Cutkosky and I. Kao, "Computing and controlling compliance of a robotic hand," *IEEE transactions on robotics and automation*, vol. 5, no. 2, pp. 151–165, 1989.
- [7] S.-F. Chen and I. Kao, "Conservative congruence transformation for joint and cartesian stiffness matrices of robotic hands and fingers," *The International Journal of Robotics Research*, vol. 19, no. 9, pp. 835–847, 2000.
- [8] I. Sharf, "Active damping of a large flexible manipulator with a shortreach robot," in *Proc. American Control Conference*, vol. 5, pp. 3329–3333, 1995.
- [9] D. W. Cannon, D. P. Magee, W. J. Book, and J. W. Lew, "Experimental study on micro/macro manipulator vibration control," in *Proc. IEEE Int'l Conf. on Robotics and Automation*, 1996, pp. 2549–2554.
- [10] T. W. Yang, W. L. Xu, and J. D. Han, "Dynamic compensation control of flexible macro-micro manipulator systems," *IEEE Transactions on Control Systems Technology*, vol. 18, no. 1, pp. 143–151, 2010.
- [11] T. Yang, Z. Sun, S. Tso, and W. Xu, "Trajectory control a flexible space manipulator utilizing a macro-micro architecture," in *2003 IEEE International Conference on Robotics and Automation (Cat. No.03CH37422)*, vol. 2, 2003, pp. 2522–2528 vol.2.
- [12] J. Lew, D. Trudnowski, M. Evans, and D. Bennett, "Micro manipulator motion control to suppress macro manipulator structural vibrations," in *Proceedings of 1995 IEEE International Conference on Robotics and Automation*, vol. 3, 1995, pp. 3116–3120 vol.3.
- [13] L. E. George and W. J. Book, "Inertial vibration damping control for a flexible base manipulator," in *ASME International Mechanical Engineering Congress and Exposition*, vol. 36290, 2002, pp. 347–354.
- [14] J. Y. Lew, and S. M. Moon, "A simple active damping control for compliant base manipulators," *IEEE Transaction on Mechatronics*, vol. 6, no. 3, pp. 305–310, 2001.
- [15] J. Lin, Z. Z. Huang, and P. H. Huang, "An active damping control of robot manipulators with oscillatory bases by singular perturbation approach," *Journal of Sound and Vibration*, vol. 304, no. 12, pp. 345–360, 2007.
- [16] D. N. Nenchev, K. Yoshida, P. Vichitkulsawat, and M. Uchiyama, "Reaction null-space control of flexible structure mounted manipulator systems," *IEEE Trans. on Robotics and Automation*, vol. 15, no. 6, pp. 1011–1023, 1999.
- [17] F. Beck, G. Garofalo, and C. Ott, "Vibration control for manipulators on a translationally flexible base," in *2019 International Conference on Robotics and Automation (ICRA)*, 2019, pp. 4451–4457.
- [18] G. Garofalo, F. Beck, J. Klodmann, and C. Ott, "On the control of translationally flexible base manipulators," in *2020 European Control Conference (ECC)*, 2020, pp. 867–874.
- [19] N. Hara, D. Nenchev, Q. Sun, and D. Sato, "Momentum conserving path tracking through dynamic singularities with a flexible-base redundant manipulator," in *2010 IEEE/RSJ International Conference on Intelligent Robots and Systems*, 2010, pp. 5392–5397.
- [20] M.-A. Bégin, R. Poon, and I. Hunter, "Streamlined tuning procedure for stable pid control of flexible-base manipulators," *IEEE Robotics and Automation Letters*, vol. 6, no. 4, pp. 7413–7420, 2021.
- [21] M. Salehi and G. Vossoughi, "Impedance control of flexible base mobile manipulator using singular perturbation method and sliding mode control law," *International Journal of Control, Automation, and Systems*, vol. 6, no. 5, pp. 677–688, 2008.
- [22] T. Wimbock, D. Nenchev, A. Albu-Schäffer, and G. Hirzinger, "Experimental study on dynamic reactionless motions with dlr's humanoid robot justin," in *Proc. IEEE/RSJ International Conference on Intelligent Robots and Systems*, 2009, pp. 5481–5486.
- [23] L. Roveda, F. Vicentini, N. Pedrocchi, and L. M. Tosatti, "Force-tracking impedance control for manipulators mounted on compliant bases," in *2014 IEEE International Conference on Robotics and Automation (ICRA)*, 2014, pp. 760–765.
- [24] L. Roveda, F. Vicentini, N. Pedrocchi, F. Braghin, and L. M. Tosatti, "Impedance shaping controller for robotic applications involving interacting compliant environments and compliant robot bases," in *2015 IEEE International Conference on Robotics and Automation (ICRA)*, 2015, pp. 2066–2071.
- [25] T. Yoshikawa, K. Harada, and A. Matsumoto, "Hybrid position/force control of flexible-macro/rigid-micro manipulator systems," *IEEE Transactions on Robotics and Automation*, vol. 12, no. 4, pp. 633–630, 1996.
- [26] Y. Hou and M. T. Mason, "Robust execution of contact-rich motion plans by hybrid force-velocity control," in *2019 International Conference on Robotics and Automation (ICRA)*, 2019, pp. 1933–1939.
- [27] M. Iskandar, C. Ott, A. Albu-Schäffer, B. Siciliano, and A. Dietrich, "Hybrid force-impedance control for fast end-effector motions," *IEEE Robotics and Automation Letters*, vol. 8, no. 7, pp. 3931–3938, 2023.
- [28] F. Ruggiero, V. Lippiello, and B. Siciliano, "Nonprehensile dynamic manipulation: A survey," *IEEE Robotics and Automation Letters*, vol. 3, no. 3, pp. 1711–1718, 2018.
- [29] J. Moura, T. Stouraitis, and S. Vijayakumar, "Non-prehensile planar manipulation via trajectory optimization with complementarity constraints," in *2022 International Conference on Robotics and Automation (ICRA)*, 2022, pp. 970–976.
- [30] J.-P. Sleiman, F. Farshidian, M. V. Minniti, and M. Hutter, "A unified mpc framework for whole-body dynamic locomotion and manipulation," *IEEE Robotics and Automation Letters*, vol. 6, no. 3, pp. 4688–4695, 2021.
- [31] G. Zhang, S. Ma, and Y. Li, "Nonprehensile pushing manipulation strategies for a multi-limb robot," in *2018 IEEE/RSJ International Conference on Intelligent Robots and Systems (IROS)*, 2018, pp. 1–9.

- [32] G. Zhang, S. Ma, Y. Shen, and Y. Li, "A motion planning approach for nonprehensile manipulation and locomotion tasks of a legged robot," *IEEE Transactions on Robotics*, vol. 36, no. 3, pp. 855–874, 2020.
- [33] S. Liu, H. Chai, R. Song, Y. Li, Y. Li, Q. Zhang, P. Fu, J. Liu, and Z. Yang, "Contact force/motion hybrid control for a hydraulic legged mobile manipulator via a force-controlled floating base," *IEEE/ASME Transactions on Mechatronics*, vol. 29, no. 3, pp. 2316–2326, 2024.
- [34] V. Morlando, M. Selvaggio, and F. Ruggiero, "Nonprehensile object transportation with a legged manipulator," in *2022 International Conference on Robotics and Automation (ICRA)*, 2022, pp. 6628–6634.
- [35] A. Rigo, M. Hu, S. K. Gupta, and Q. Nguyen, "Hierarchical optimization-based control for whole-body loco-manipulation of heavy objects," in *2024 IEEE International Conference on Robotics and Automation (ICRA)*, 2024, pp. 15 322–15 328.
- [36] M. Sombolstan, Y. Chen, and Q. Nguyen, "Adaptive force-based control for legged robots," in *2021 IEEE/RSJ International Conference on Intelligent Robots and Systems (IROS)*, 2021, pp. 7440–7447.
- [37] A. Rigo, Y. Chen, S. K. Gupta, and Q. Nguyen, "Contact optimization for non-prehensile loco-manipulation via hierarchical model predictive control," in *2023 IEEE International Conference on Robotics and Automation (ICRA)*, 2023, pp. 9945–9951.
- [38] A. Konno, Y. Hwang, S. Tamada, and M. Uchiyama, "Working postures for humanoid robots to generate large manipulation force," in *2005 IEEE/RSJ International Conference on Intelligent Robots and Systems*, 2005, pp. 2548–2553.
- [39] M. Murooka, S. Nozawa, Y. Kakiuchi, K. Okada, and M. Inaba, "Whole-body pushing manipulation with contact posture planning of large and heavy object for humanoid robot," in *2015 IEEE International Conference on Robotics and Automation (ICRA)*, 2015, pp. 5682–5689.
- [40] J. Li and Q. Nguyen, "Kinodynamic pose optimization for humanoid loco-manipulation," in *2023 IEEE-RAS 22nd International Conference on Humanoid Robots (Humanoids)*, 2023, pp. 1–8.
- [41] F. Abi-Farraj, B. Henze, C. Ott, P. R. Giordano, and M. A. Roa, "Torque-based balancing for a humanoid robot performing high-force interaction tasks," *IEEE Robotics and Automation Letters*, vol. 4, no. 2, pp. 2023–2030, 2019.
- [42] M. P. Polverini, A. Laurenzi, E. M. Hoffman, F. Ruscelli, and N. G. Tsagarakis, "Multi-contact heavy object pushing with a centaur-type humanoid robot: Planning and control for a real demonstrator," *IEEE Robotics and Automation Letters*, vol. 5, no. 2, pp. 859–866, 2020.
- [43] S. Komatsu, Y. Kakiuchi, S. Nozawa, Y. Kojio, F. Sugai, K. Okada, and M. Inaba, "Tool force adaptation in soil-digging task for humanoid robot," in *2017 IEEE-RAS 17th International Conference on Humanoid Robotics (Humanoids)*, 2017, pp. 378–383.
- [44] T. Murooka, R. Shigematsu, K. Kojima, F. Sugai, Y. Kakiuchi, K. Okada, and M. Inaba, "Whole-body posture generation by adjusting tool force with cog movement: Application to soil digging," in *2019 IEEE-RAS 19th International Conference on Humanoid Robots (Humanoids)*, 2019, pp. 202–207.
- [45] S. Komatsu, Y. Nagamatsu, T. Ishikawa, T. Shirai, K. Kojima, Y. Kakiuchi, F. Sugai, K. Okada, and M. Inaba, "Humanoid robot's force-based heavy manipulation tasks with torque-controlled arms and wrist force sensors," in *2019 IEEE/RSJ International Conference on Intelligent Robots and Systems (IROS)*, 2019, pp. 3055–3062.
- [46] A. Ajoudani, J. Lee, A. Rocchi, M. Ferrati, E. M. Hoffman, A. Settini, D. G. Caldwell, A. Bicchi, and N. G. Tsagarakis, "A manipulation framework for compliant humanoid coman: Application to a valve turning task," in *2014 IEEE-RAS International Conference on Humanoid Robots*, 2014, pp. 664–670.
- [47] D. E. Orin, A. Goswami, and S.-H. Lee, "Centroidal dynamics of a humanoid robot," *Autonomous robots*, vol. 35, pp. 161–176, 2013.
- [48] H. Dai, A. Valenzuela, and R. Tedrake, "Whole-body motion planning with centroidal dynamics and full kinematics," in *2014 IEEE-RAS International Conference on Humanoid Robots*, 2014, pp. 295–302.
- [49] J. Ahn, J. Yoon, J. Lee, and D. Lee, "Model-free optimal estimation and sensor placement framework for elastic kinematic chain," in *Proc. IEEE Int'l Conference on Robotics and Automation*, 2019, pp. 8776–8782.
- [50] S. G. Johnson, "The NLopt nonlinear-optimization package," <https://github.com/stevengj/nlopt>, 2007.